

## Article

# Effects of Aluminosilicate Gel Treatment and TiO<sub>2</sub> Loading on Photocatalytic Properties of Au–TiO<sub>2</sub>/Zeolite Y

Gabriela Petcu<sup>1,\*</sup>, Florica Papa<sup>1</sup>, Elena Maria Anghel<sup>1</sup> , Irina Atkinson<sup>1</sup>, Silviu Preda<sup>1</sup>, Simona Somacescu<sup>1</sup>, Daniela C. Culita<sup>1</sup> , Adriana Baran<sup>1</sup>, Elena Madalina Ciobanu<sup>1</sup> , Luiza Maria Jecu<sup>2</sup>, Mariana Constantin<sup>2</sup> and Viorica Parvulescu<sup>1,\*</sup>

<sup>1</sup> Institute of Physical Chemistry “Ilie Murgulescu” of the Romanian Academy, 202 Splaiul Independentei, 060021 Bucharest, Romania; manghel@icf.ro (E.M.A.); iatkinson@icf.ro (I.A.); mciobanu@icf.ro (E.M.C.)

<sup>2</sup> National Institute for Research & Development in Chemistry and Petrochemistry-ICECHIM, Spl. Independentei 202, 060021 Bucharest, Romania

\* Correspondence: gpetcu@icf.ro (G.P.); vpirvulescu@icf.ro (V.P.)

**Abstract:** The present work reports the synthesis of efficient Ti–Au/zeolite Y photocatalysts by different processing of aluminosilicate gel and studies the effect of titania content on the structural, morphological, textural, and optical properties of the materials. The best characteristics of zeolite Y were obtained by aging the synthesis gel in static conditions and mixing the precursors under magnetic stirring. Titania (5, 10, 20%) and gold (1%) species were incorporated in zeolite Y support by the post-synthesis method. The samples were characterized by X-ray diffraction, N<sub>2</sub>-physisorption, SEM, Raman, UV–Vis and photoluminescence spectroscopy, XPS, H<sub>2</sub>-TPR, and CO<sub>2</sub>-TPD. The photocatalyst with the lowest TiO<sub>2</sub> loading shows only metallic Au on the outermost surface layer, while a higher content favors the formation of additional species such as: cluster type Au, Au<sup>1+</sup>, and Au<sup>3+</sup>. A high TiO<sub>2</sub> content contributes to increasing the lifetime of photogenerated charge carriers, and the adsorption capacity of the pollutant. Therefore, an increase in the photocatalytic performances (evaluated in degradation of amoxicillin in water under UV and visible light) was evidenced with the titania content. The effect is more significant in visible light due to the surface plasmon resonance (SPR) effect of gold interacting with the supported titania.

**Keywords:** aluminosilicate gel; zeolite Y; Ti–Au zeolite Y; photocatalysis; surface plasmon resonance; effect of TiO<sub>2</sub> loading; photodegradation; amoxicillin



**Citation:** Petcu, G.; Papa, F.; Anghel, E.M.; Atkinson, I.; Preda, S.; Somacescu, S.; Culita, D.C.; Baran, A.; Ciobanu, E.M.; Jecu, L.M.; et al. Effects of Aluminosilicate Gel Treatment and TiO<sub>2</sub> Loading on Photocatalytic Properties of Au–TiO<sub>2</sub>/Zeolite Y. *Gels* **2023**, *9*, 503. <https://doi.org/10.3390/gels9060503>

Academic Editors: Yuesheng Li, Avinash J. Patil, Xiaojie Yang, Jun Xing and Yiwan Huang

Received: 19 May 2023  
Revised: 9 June 2023  
Accepted: 16 June 2023  
Published: 20 June 2023



**Copyright:** © 2023 by the authors. Licensee MDPI, Basel, Switzerland. This article is an open access article distributed under the terms and conditions of the Creative Commons Attribution (CC BY) license (<https://creativecommons.org/licenses/by/4.0/>).

## 1. Introduction

The importance of faujasite-based catalysts has led to a growing interest in facile synthesis procedures that allow for preparing high-performance materials with improved catalytic properties. The performance of zeolites is greatly influenced by their size and shape, morphological homogeneity being desirable [1–3]. It is well known that in zeolite synthesis, the mixing of aluminate and silicate in a high pH medium led to the formation of hydrogel. This behavior was explained by the spontaneously bonding in a first stage of some aluminate ions to the silica oligomers, following multiple processes of dissolution and regeneration of the gel until the equilibrium state is reached [4]. Previous studies evidenced the importance of the aging process on gel chemistry in the synthesis of zeolite materials by controlling the nucleation and crystal growth [5]. Finding the parameters that determine the crystal morphology and size is essential in tailoring the properties of zeolites [1] which are often used as supports in obtaining photocatalysts because of their specific advantages such as structure, stability, high surface area, uniform pores, and channels with high adsorption capacity, acid-basic properties, ion exchange ability, and electric field of the framework [6–8].

TiO<sub>2</sub> is a widely studied semiconductor due to its well-known advantages and potential application in different fields such as solar energy conversion, antibacterial treatments,

and heterogeneous photocatalysis [9–12]. However, TiO<sub>2</sub> applications are limited because of its large energy band gap and the tendency of particles to agglomerate in aqueous media with a reduction in the exposed surface area. The narrowing of the energy band gap was achieved by TiO<sub>2</sub> doping with various metals or nonmetal species [13–18]. A method to diminish agglomerations is the immobilization of TiO<sub>2</sub> nanoparticles on a support framework, such as zeolites [19–22]. In this case, the surface chemistry of the support plays a decisive role in photocatalytic activity and stability [23]. The photocatalysts thus obtained showed, in most cases, a higher activity than unsupported TiO<sub>2</sub>, assigned to the synergism between the electron-rich nature and large surface area of the zeolites which facilitates an excellent dispersion of TiO<sub>2</sub> nanoparticles, to adsorption of organic substrates on the zeolite support and to the effective separation of the photogenerated electrons and holes by the electric field of the zeolite framework [24]. The adsorption of pollutants on the photocatalyst is a very important step because charge carriers resulted under irradiation have a short lifetime, so the presence of pollutant molecules adsorbed on the surface have a higher probability to interact with the active sites. A significant problem of TiO<sub>2</sub>-loaded zeolite is the structural collapse of the zeolite structure when the optimum TiO<sub>2</sub> loading is exceeded. Thus, TiO<sub>2</sub>/zeolite Na-A catalyst was successfully synthesized by a slightly modified sol–gel technique and the effects of TiO<sub>2</sub> loading on structural, optical, adsorptive, and photocatalytic properties were evaluated [6]. The obtained results showed a small effect on the zeolite structure, decreasing of band gap energy with TiO<sub>2</sub> loading, and increasing photocatalytic activity.

The Au–TiO<sub>2</sub> system has attracted considerable attention because of the high and stable photocatalytic activity that can be achieved under both UV and visible light excitation [25]. TiO<sub>2</sub> was considered to be a good support for Au photocatalysts due to the strong interaction metal-support, chemical stability, and acid-base properties [26]. The main role of TiO<sub>2</sub> utilized in photocatalysis is to generate, under light irradiation, charge carriers and reactive oxygen species (ROS). The gold nanoparticles influence the activation of TiO<sub>2</sub> by plasmonic resonance energy transfer or by “hot electrons” injected into the conduction band of the TiO<sub>2</sub> support [27]. The surface and interface properties of plasmonic Au/TiO<sub>2</sub> nanocatalysts play a critical role in determining their performance in photocatalytic oxidation reactions [28,29].

The previous studies showed that the dispersion of titanium species and gold significantly influences the catalytic activity, durability, and selectivity in amoxicillin photodegradation [20]. These properties were significantly influenced by the support surface area, porous structure, and morphology which have modulated the electronic Au–TiO<sub>2</sub> interaction. The synergistic effect between Au–TiO<sub>2</sub> and supports was the result of an intimate contact between components, determined by the dispersion of titania, and implicitly of gold species on the support.

In this study, new active photocatalysts were obtained by the manufacturing of aluminosilicate gel to obtain the zeolite Y with a crystalline structure, and its modification with various amounts of TiO<sub>2</sub> (5, 10, 20%) and gold (1%) species. For this purpose, the effects of the experimental conditions during the processing of the synthesis gel on the structural and morphological properties of zeolite Y were evaluated. Previous studies showed the formation of zeolite Y crystalline phase during the sol–gel process [30]. Compared to the other porous supports used (MCM-48, KIT-6, SBA-15, hierarchical zeolite Y), microporous zeolite Y with the same concentration of TiO<sub>2</sub> (10%) seems to have a lower activity [20]. This is probably the reason why Au–TiO<sub>2</sub> photocatalysts supported on zeolite Y have been less studied. In this context, the present work aimed to evaluate the effect of TiO<sub>2</sub> loading on the interaction with the subsequently immobilized gold species (especially the optical properties) in order to improve the photocatalytic activity of these materials. For the new samples obtained, the test reaction was also amoxicillin photodegradation.

## 2. Results and Discussion

### 2.1. Effect of Aluminosilicate Gel Treatment

In order to obtain high-performance materials for photocatalytic applications, the hydrogel spontaneously obtained after mixing aluminate and silicate was differently treated. Thus, the influence of the reactants mixing method (magnetic/assisted by ultrasound) and the effect of stirring during the hydrogel aging were studied. Structural and morphological changes that occur by varying the experimental conditions during the aging of aluminosilicate hydrogel used to synthesize zeolite Y were investigated by X-ray diffraction, Raman spectroscopy, and scanning electron microscopy.

#### 2.1.1. XRD Analysis

The X-ray diffraction patterns recorded for the powders obtained by different gel treatment procedures are summarized in Figure 1. The detectable diffraction peaks correspond to (111), (220), (311), (331), (333), (440), (620), (551), (731), (822), (660), (842), and (862) planes of the typical structure of faujasite Na-Y (ICDD 00-038-0239) [31]. The changes in intensity depending on the treatment applied to the synthetic gel indicate some variation in the crystal structure. Thus, the mixing of the reactants under magnetic stirring and aging of the aluminosilicate gel in the static mode (the second route, as described in the sample preparation section) led to the formation of zeolite Y with the highest degree of crystallinity.

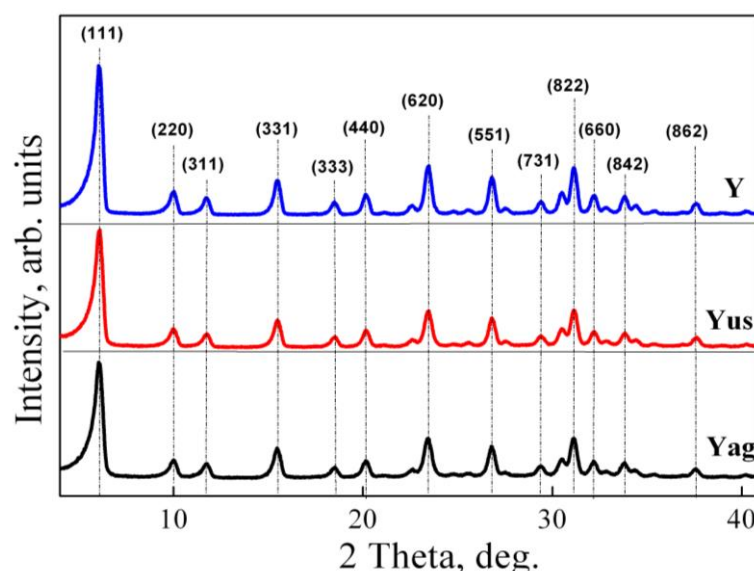


**Figure 1.** Wide-angle X-ray diffraction patterns of zeolite Y obtained by different treatments of aluminosilicate hydrogel during the aging step.

#### 2.1.2. Raman Spectroscopy

The UV-Raman spectra of the zeolite powders obtained by different treatments of aluminosilicate gel are illustrated in Figure 2. For all the samples, the spectral features of zeolite Y at 372, ~500, 1006, and 1081  $\text{cm}^{-1}$  were noticed, assigned to bending vibrations of the six- and four-membered  $\text{SiO}_4$  rings and asymmetric stretching mode of the T-O linkages (T stands for Al and/or Si) [32]. The asymmetric stretching modes of T-O bonds at 1063  $\text{cm}^{-1}$  in the  $\text{Y}_{\text{ag}}$  spectrum are intermediate to the ones for X zeolite (1075  $\text{cm}^{-1}$ ) and Y zeolite (1055  $\text{cm}^{-1}$ ) [32] pointing out that the Si/Al ratio could be slightly modified in the  $\text{Y}_{\text{ag}}$  sample. Analogous spectral features to Y were depicted for the  $\text{Y}_{\text{us}}$  sample. This is probably due to the entrainment of more aluminosilicate by stirring during aging which leads to a slight change in the Si/Al ratio.

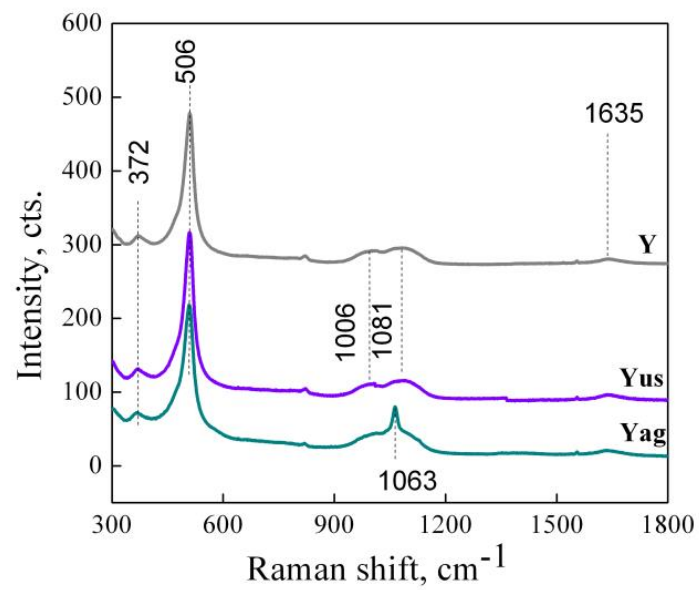


**Figure 2.** UV-Raman spectra of the zeolite materials obtained by different treatment of aluminosilicate gel.

### 2.1.3. SEM Images

SEM images of zeolite Y powders obtained by different treatments of synthesis gel are illustrated in Figure 3.

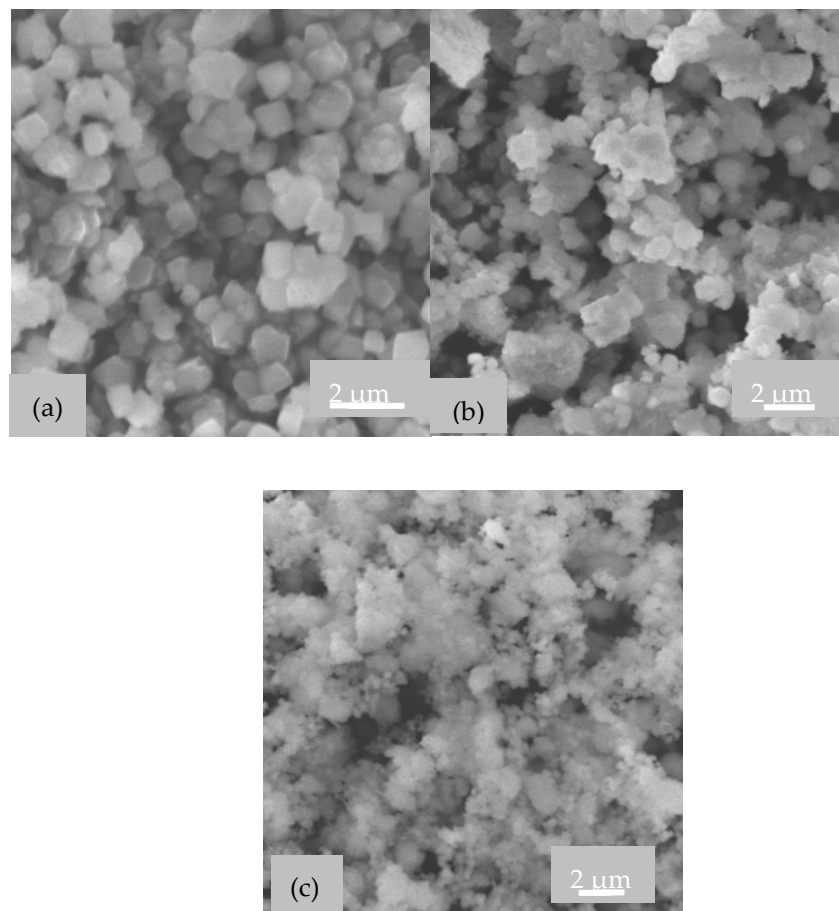


**Figure 3.** SEM images of zeolite (a) Y, (b) Yus, (c) Yag.

It is obvious that the morphology of zeolite Y powders can be controlled by manufacturing the aluminosilicate hydrogel. Thus, octahedral particles, with smooth faces, specific to zeolite Y were obtained using the classical stirring method and aging the gel in the static mode. Smaller crystals were obtained in the case of gel aging under stirring (Figure 3b), due to the fact that accelerated mass transfer led to a rapid supersaturation [5]. Furthermore, an inhomogeneous morphology with slightly rounded particles and some agglomerates were noticed. These morphologies correspond to a lower degree of crystallinity, as was also highlighted with the help of the X-ray diffraction patterns shown in Figure 1.

## 2.2. Effect of TiO<sub>2</sub> Loading

The results presented in Section 2.1 pointed out the possibility to design the aluminosilicate hydrogel by changing the experimental conditions, leading to obtaining faujasite Y materials with suitable properties for photocatalysis. Further, it was chosen the material obtained by the second route (see the representation illustrated in the sample preparation section), modified with different TiO<sub>2</sub> loadings (5%, 10%, 20%) and Au (only 1%) reactive species and characterized by various techniques.

### 2.2.1. XRD Analysis

Wide-angle X-ray patterns recorded for the synthesized photocatalysts are illustrated in Figure 4. It can be noticed that all three samples with different titania loading and 1% Au have comparable diffraction patterns with the zeolite support, suggesting preservation of the crystalline structure of microporous zeolite Y after Ti and Au incorporation.

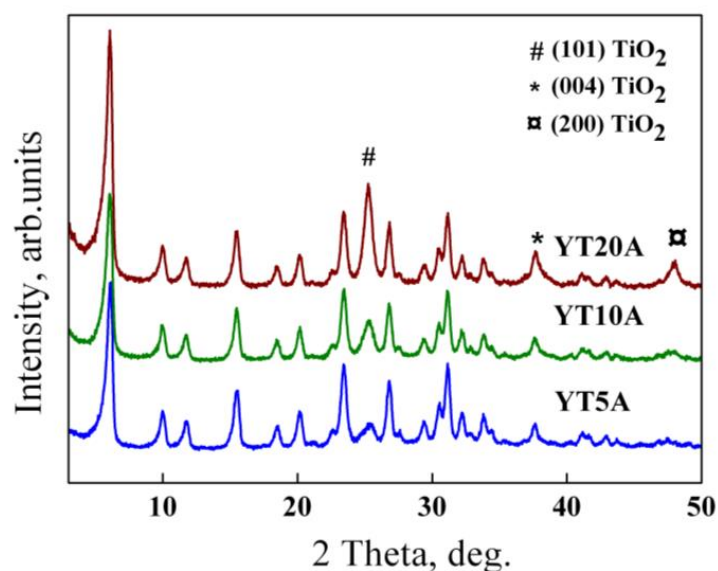


**Figure 4.** Wide-angle X-ray diffraction patterns of the prepared Au–Ti samples with different TiO<sub>2</sub> loading and corresponding zeolite Y support.

No diffraction peaks assigned to the gold-based compounds were identified in the X-ray diffractograms of the samples. It can be explained by the high dispersion of gold nanoparticles and also by their low relative concentration (<1%), below the detection limit of the instrument [33]. However, the presence of gold species together with titanium was highlighted by means of EDS analysis for YT10A sample (see Figure S1C from Ref. [20]).

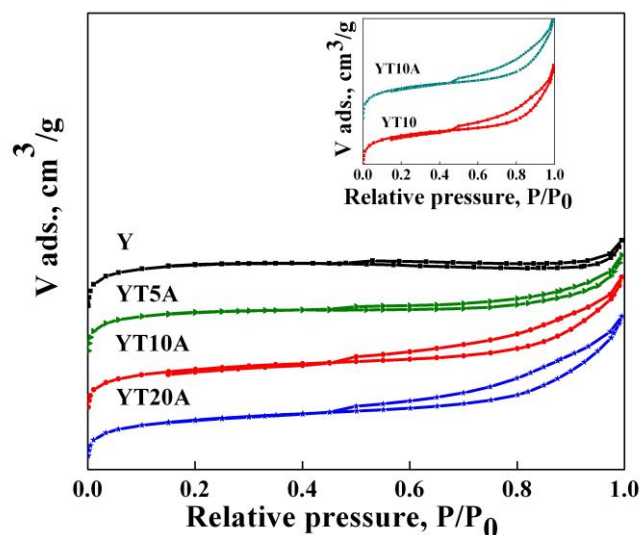
For all three samples (YT5A, YT10A, YT20A) was observed the presence of three distinct diffraction lines at  $2\theta \approx 25.2^\circ$ ,  $37.8^\circ$ , and  $48.1^\circ$ , corresponding to (101), (004), and (200) crystal planes of anatase TiO<sub>2</sub> phase (Figure 4). Increasing titania loadings on zeolite Y support (5%, 10%, 20%) caused an increase in anatase diffraction line intensities. The average crystallite size, estimated using the Scherrer equation along the (101) direction, follows a similar trend (Table 1).

**Table 1.** Textural and optical properties of the samples.

Sample	BET Surface Area (m <sup>2</sup> /g)	V <sub>pore</sub> (cm <sup>3</sup> /g)	Pore Size (nm)	TiO <sub>2</sub> Crystallite Size (nm)	Band Gap Energy (eV)
YT5	850	0.102	1.6	9.9	3.09
YT5A	856	0.104	1.6	10.0	3.22
YT10	678	0.107	1.8	10.2	3.17
YT10A	699	0.109	1.8	10.3	3.20
YT20	507	0.114	2.0	12.1	3.14
YT20A	572	0.154	2.0	12.3	3.15

### 2.2.2. Textural Analysis

The N<sub>2</sub> adsorption–desorption isotherms of the Ti–Au photocatalysts are presented in Figure 5. According to the IUPAC classification, the synthesized samples show a combination of type I and IV isotherms with H3 and H4 hysteresis loops [34]. In contrast to the case of using ordered mesoporous silica as support for the synthesis of Ti–Au photocatalysts, studied previously by our group [20], for which the shape and pores dimensions were preserved after titanium and gold immobilization, in the present work was observed a hysteresis loop came out after TiO<sub>2</sub> immobilization. It can be explained by the formation of mesopores among TiO<sub>2</sub> nanoparticles supported on microporous zeolite Y. BET surface areas, pore volume, and size after each impregnation step are summarized in Table 1. High values of the specific surfaces were obtained compared to other similar cases reported in the literature. For example, the BET surface area recorded for YT10A sample was 699 m<sup>2</sup>/g, unlike values such as 462 and 561 obtained for photocatalytic materials based on USY with 12% TiO<sub>2</sub> and 3% gold [35]. Generally, a gradual decrease in BET surface area was noticed after titania loadings, while further immobilization of gold led to a slight increase in BET surface area.

**Figure 5.** The nitrogen adsorption–desorption isotherms of the synthesized samples.

### 2.2.3. SEM Images

The morphology of the synthesized samples was investigated by scanning electron microscopy, and the obtained images are presented in Figure 6. No change of morphology was observed after the impregnations of supports. Thus, for a high concentration of TiO<sub>2</sub> (20%), YT20A sample, the preservation of octahedral morphology with smooth surfaces, specific to zeolite Y, and no aggregates or any other defects were observed.

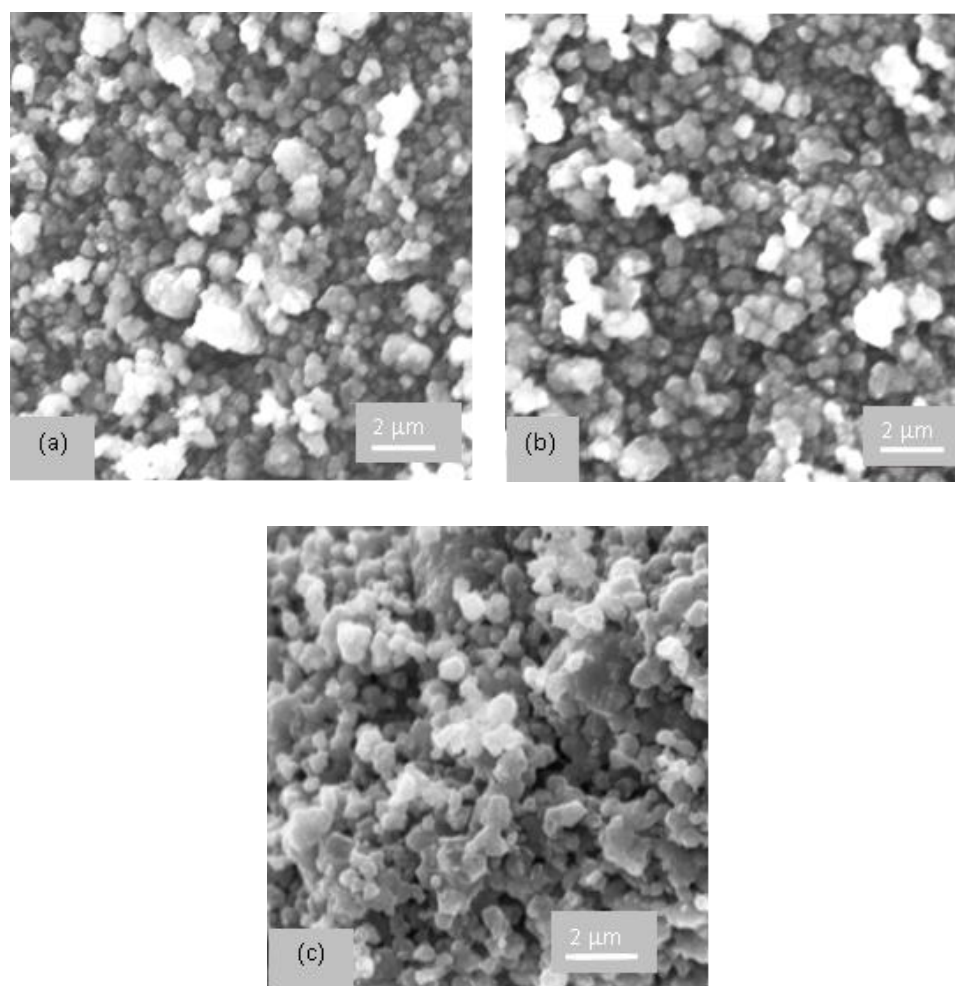


**Figure 6.** SEM images of (a) YT5A, (b) YT10A, and (c) YT20A photocatalysts.

#### 2.2.4. XPS Results

XPS spectroscopy indicates low concentrations of gold on the sample surface (<1%), as the recorded photoelectron spectra are very noisy, even though there was a large number of runs recorded during data acquisition. Moreover, the Au4f spectra have a “band-like” shape which suggests the presence of different gold species accommodated under the experimental spectra envelope.

The Au4f spectra recorded for the samples (Figure 7) showed the presence of different types of gold species depending on TiO<sub>2</sub> loading.

The interaction between gold nanoparticles and titanium species varied with the amount of immobilized TiO<sub>2</sub>. Thus, the sample with the lowest TiO<sub>2</sub> content (YT5A) shows only Au metallic nanoparticles and Au<sup>3+</sup> ions on the outermost surface layer. For a higher concentration of TiO<sub>2</sub> (YT10A and YT20A samples), very small Au clusters (Au NCs) as well as Au<sup>1+</sup> ions were additionally identified [36,37]. It is worth outlining that for the samples with higher TiO<sub>2</sub> content (10, 20%) the relative concentrations of the aforementioned species do not reveal significant changes. As shown by the XPS data (Table 2) [38], depending on the concentration of TiO<sub>2</sub> supported on the zeolite, the obtained gold species were different. A higher relative concentration of Au metallic nanoparticles was evidenced for the YT5A sample with the smallest TiO<sub>2</sub> crystallite size (Table 1) which most likely contributes to more intimate contact with immobilized gold. Thus, a strong interaction takes place which means an electron transfer between the support modified with TiO<sub>2</sub> and the Au<sup>3+</sup> species (used for impregnation), reducing them to metallic Au.

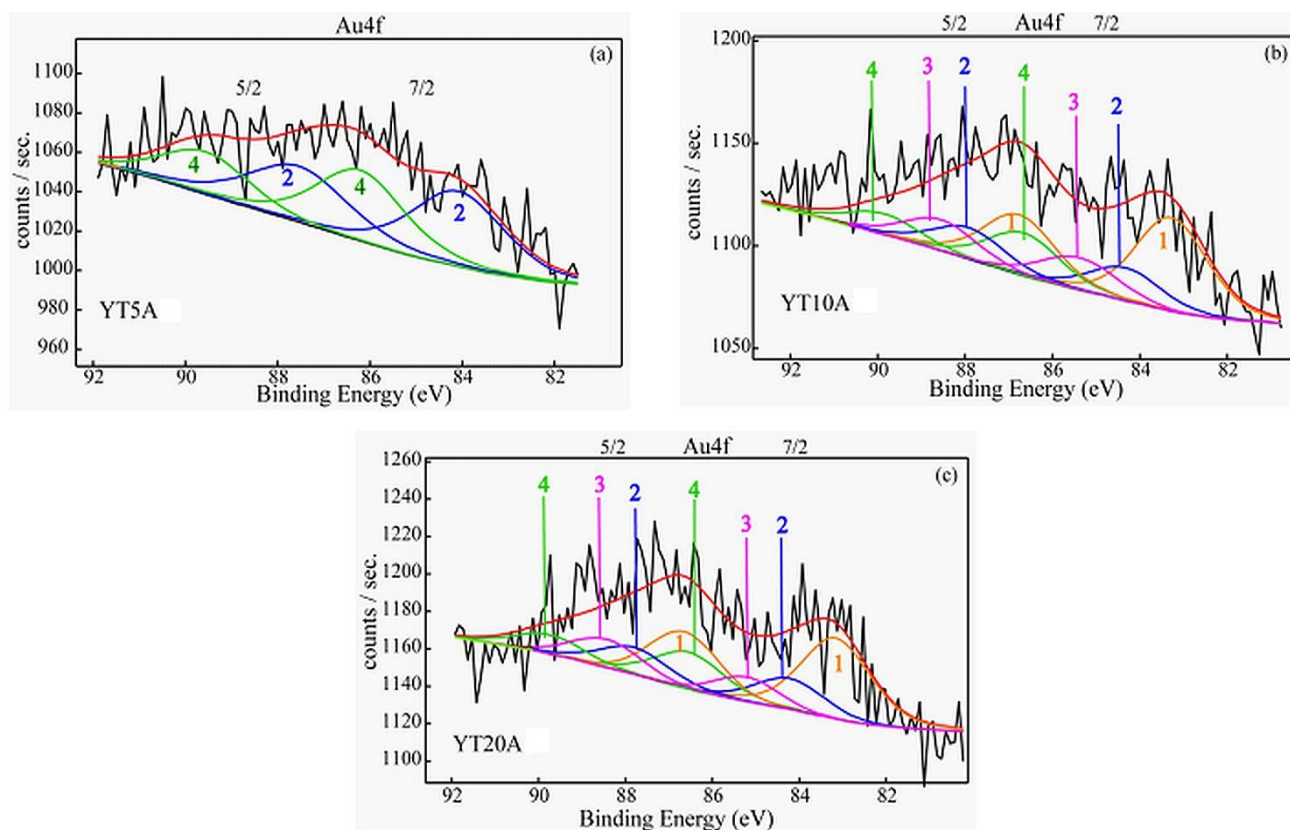


**Figure 7.** (a–c) Au 4f (7/2, 5/2) high resolution, deconvoluted XPS spectra for the synthesized samples.

**Table 2.** XPS data: binding energies (BEs) and the quantitative assessment.

Sample	Binding Energy (eV)				Au Chemical Species Rel. Conc.				
	Au4f/2 Metallic nps	Au4f/2 Clusters	Au4f/2 Au+	Au4f/2 Au3+	Au Metallic nps	Clusters	Au <sup>1+</sup>	Au <sup>3+</sup>	
YT5A	83.3	84.3	85.3	86.7	56.1	-	-	43.9	
YT10A	83.3	84.3	85.3	86.7	44.7	18.8	18	18.6	
YT20A	83.3	84.3	85.3	86.7	45.7	19.2	16	19	

The surface chemistry of titanium, oxygen, silicon, and aluminum was evaluated for all the samples and the results are illustrated in Figure 8a–d. The two peaks recorded for Ti 2p (Figure 8a) are assigned to Ti<sup>4+</sup> from Ti–O–Ti (lower binding energy) and Ti<sup>4+</sup> from the isolated Ti–O–Si (higher binding energy) coordination [39]. The O1s high-resolution XPS spectra (Figure 8b) present two peaks: one is attributed to the O–Si band from zeolite support (~532.5 eV), and another one, with variable intensity from lower binding energy (~531 eV), indicates the presence of oxygen bonded to Ti in TiO<sub>2</sub> species with octahedral coordination. For Si2p XPS spectra (Figure 8c), the peak located at BEs (102.3 eV) was assigned to Si–O from zeolite Y supports. Figure 8d confirms the presence of aluminum on the surface of the obtained samples.

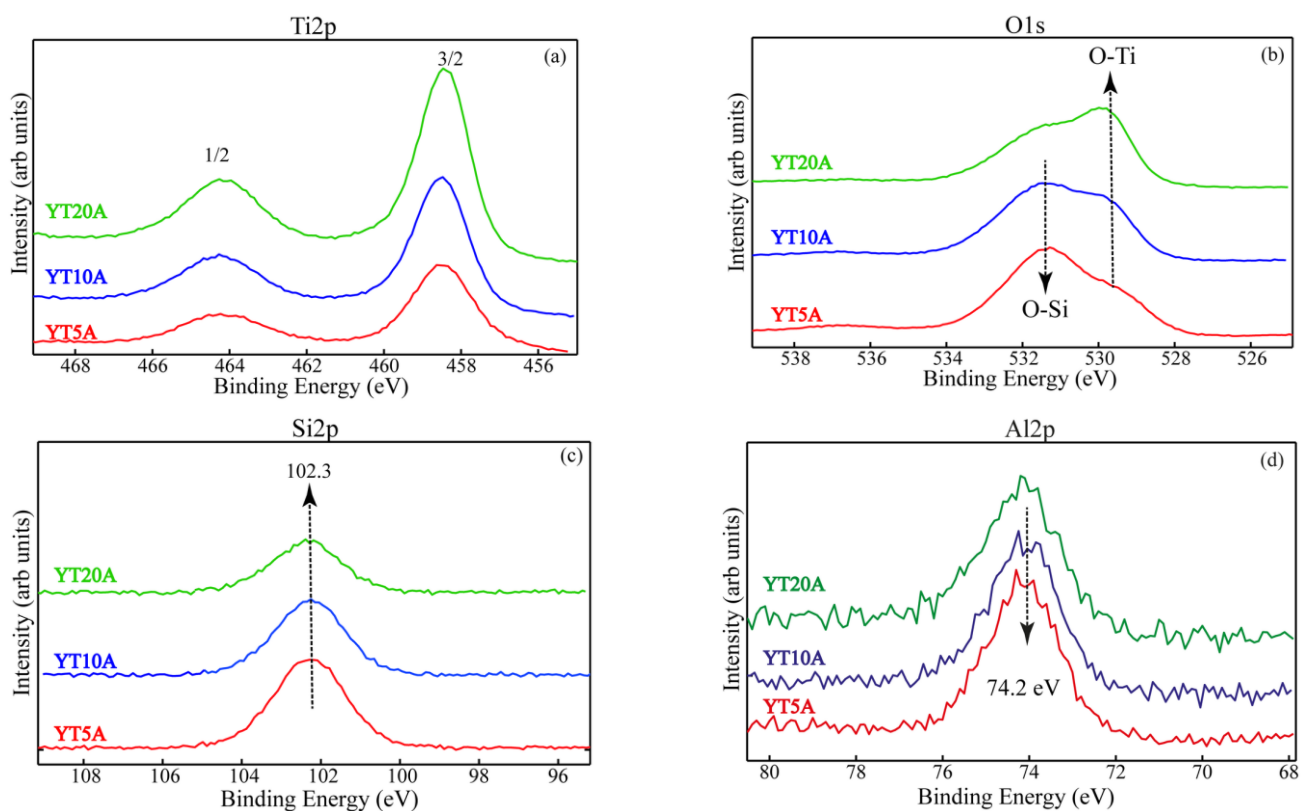


Figure 8. Ti2p (a), O1s (b), Si2p (c), and Al2p (d) superimposed high-resolution XPS spectra.

### 2.2.5. Raman Spectroscopy

The UV-Raman spectral features of zeolite Y at 372, ~500, 1006, and 1081  $\text{cm}^{-1}$  are masked by the stronger vibration modes of the framework titania [40] as rutile polymorph (611 and 826  $\text{cm}^{-1}$  due to  $A_{1g}$  and  $B_{2g}$  modes [41]). The anatase phase is also depictable in Figure 9 by the weaker shoulders at 398  $\text{cm}^{-1}$  ( $B_{1g}$ ) and 633  $\text{cm}^{-1}$  ( $E_g$ ) [41].

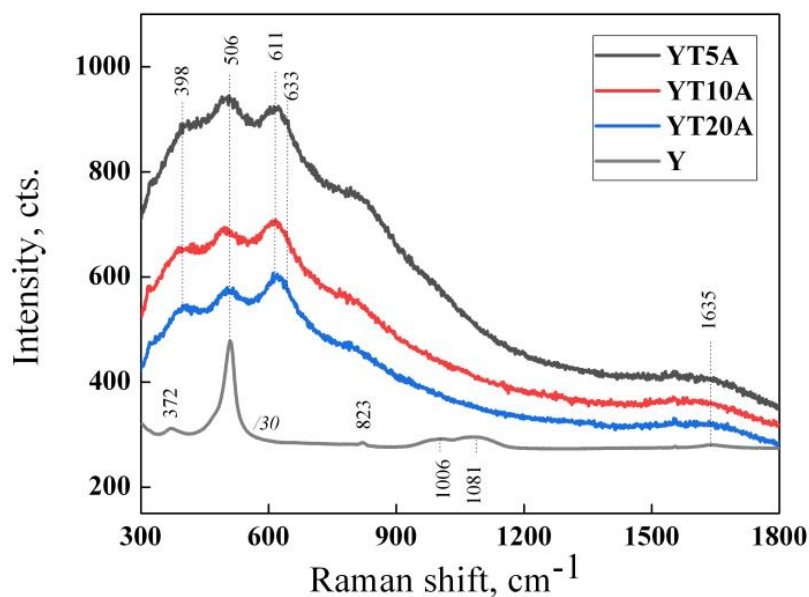
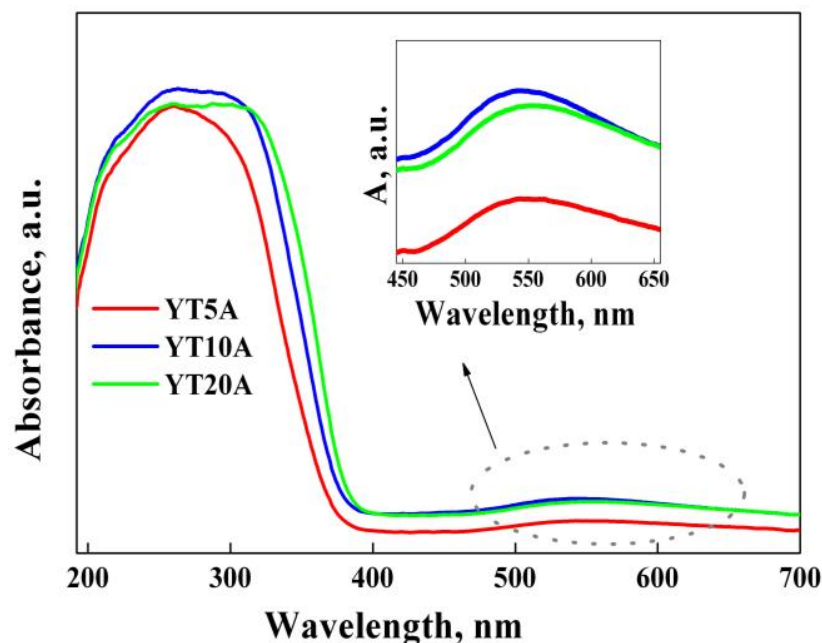


Figure 9. UV-Raman spectra of the YTxA samples ( $x = 5, 10, 20$ ) and zeolite Y.

Since the intensity of the band located at about 500  $\text{cm}^{-1}$  decreases with  $\text{TiO}_2$  loading, it points out that the surface of the Y zeolite is better covered by  $\text{TiO}_2$ .

### 2.2.6. UV–Vis Absorbance Spectroscopy

The optical properties of the synthesized materials were investigated by UV–Vis absorption spectroscopy and the obtained spectra are shown in Figure 10.



**Figure 10.** UV–Vis absorption spectra of Au–Ti photocatalysts.

An intense absorption band in the UV range was obtained for all the photocatalysts, associated with tetrahedral Ti species ( $\sim 220$  nm), octahedral Ti-oxide species ( $\sim 260$  nm), and  $\text{TiO}_2$  as agglomerations on the zeolite surface ( $>300$  nm) [42,43]. Furthermore, a red-shift of the absorption bands with titania amount was shown, corresponding to an increase in  $\text{TiO}_2$  particle size, supported by the values obtained using the Scherrer equation (Table 1). It can be explained by the quantum size effect that emerges for  $\text{TiO}_2$  species with particle size  $< 10$  nm [44]. Another band absorption with a maximum of around 550 nm was observed in the visible domain, corresponding to the local surface plasmon resonance effect of gold nanoparticles [45]. The highest intensity of this absorption band was obtained for the photocatalyst with a  $\text{TiO}_2$  content of 10%. So, this concentration can be considered as optimal for ensuring the interaction between titania with gold species. Consequently, the intensity of the Au plasmonic effect increased as follows:  $\text{YT5A} < \text{YT10A} < \text{YT20A}$ .

The indirect band gap energies were calculated using the Kubelka–Munk function by plotting  $[\text{F(R)} \cdot \text{h}\nu]^{1/2}$  versus photon energy (eV). The obtained values (Table 1) suggest a decrease in the band gap energy after titanium immobilization compared to bulk  $\text{TiO}_2$  (3.2 eV) due to the high dispersion of titania [46,47]. A slight increase in the band gap was obtained by gold immobilization, as a result of plasmonic properties of gold nanoparticles that inject electrons into the conduction band of  $\text{TiO}_2$  (Burstein–Moss (BM) effect [48]). Therefore, sufficiently high energy is needed to allow the transfer of electrons to a higher free energy level. However, the band gap values calculated for the studied samples (Table 1) were considerably lower than those reported in the literature (3.54, 3.44 eV [35]).

### 2.2.7. Photoluminescence Spectroscopy

The photoluminescence spectra recorded for Ti-modified materials before and after gold immobilization are illustrated in Figure 11a,b.

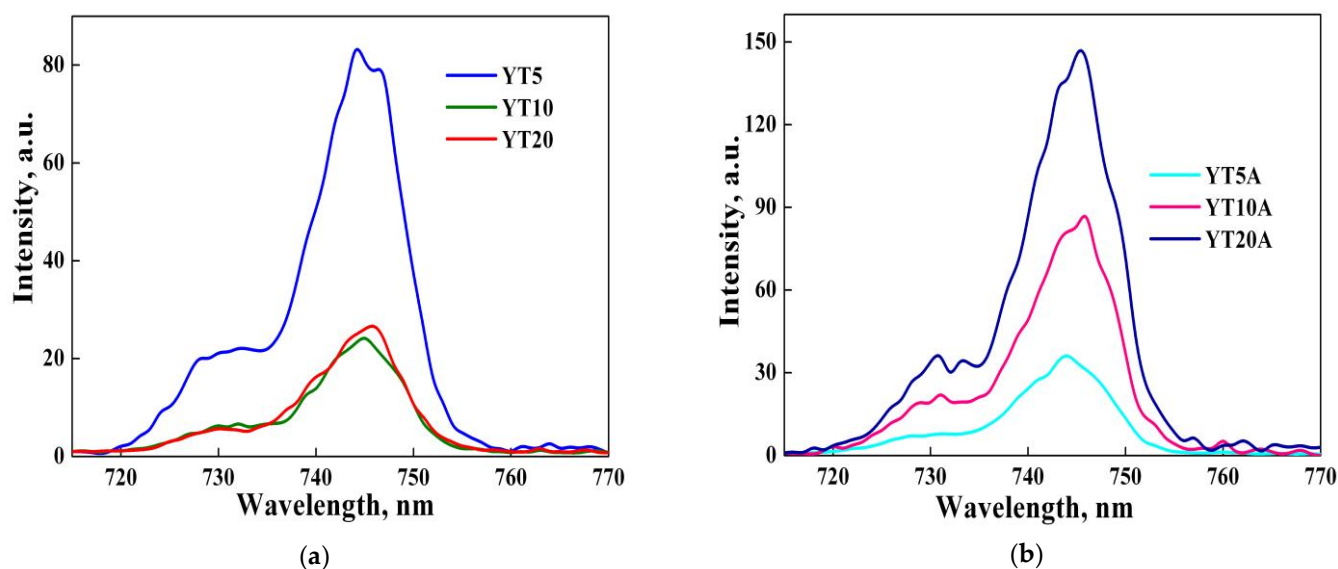


**Figure 11.** PL spectra of the YTx materials (a) and YTxA samples (b).

It was noticed a decrease in the PL emission with TiO<sub>2</sub> loading (Figure 11a), suggesting the enhancement of materials' capacity to capture photogenerated electrons, improving e<sup>-</sup>/h<sup>+</sup> separation. A better separation of electron-hole pairs in the case of higher TiO<sub>2</sub> content, ultimately means better photocatalytic properties. After gold immobilization, different behaviors were noticed (Figure 11b) depending on the type of gold species that resulted after interaction with TiO<sub>2</sub> added in various concentrations. Thus, the lowest PL emission was obtained for the YT5A sample which has only metallic gold nanoparticles and Au<sup>3+</sup> species on the surface, as XPS results showed (Table 2).

#### 2.2.8. H<sub>2</sub>-TPR Studies

The influence of titania content on the materials' reducibility was monitored by H<sub>2</sub> temperature programmed reduction (H<sub>2</sub>-TPR). The TPR profiles show (Figure 12) broad reduction peaks. These were attributed to the reduction of gold cations (Au<sup>+</sup> and Au<sup>3+</sup>), evidenced by XPS (Table 2), which interact with titanium species dispersed on supports. In the absence of Ti species, the reduction profile of the YA sample appeared as two peaks with a maximum of around 50 °C and 130 °C. The first has been assigned to the adsorption of hydrogen on zeolite Y [49] and the second to the reduction of Au<sup>3+</sup> species to Au<sup>0</sup> [50]. The 10% TiO<sub>2</sub> loading on zeolite Y (sample YT10) can hardly react with H<sub>2</sub>. Two main very weak and broad signals at around 250 °C and 650 °C were evidenced by H<sub>2</sub>-TPR profiles (inset of Figure 12). The peak located at lower temperatures was attributed to the presence of subsurface oxygen, while the signal from higher temperatures was assigned to oxygen species that are strongly chemisorbed on the surface or to a possible reduction of Ti<sup>4+</sup> to Ti<sup>3+</sup> [51]. Therefore, Au-TiO<sub>2</sub> interaction influenced the intensity and position of the reduction peaks. Two different profiles can be seen in Figure 12 for samples with different concentrations of titanium oxide. The highest peak with one maximum at 160 °C was obtained for the YT5A sample with the highest Au<sup>3+</sup> species on the surface (Table 2). Similar TPR profiles were obtained for YT10A and YT20A samples except for one shoulder at around 100 °C (of the first) and another at 240 °C observed for the last one. The difference between these samples is the loading and nature of titanium species. Generally, the weak interaction (Au cations with TiO<sub>2</sub> species) leads to reduction peaks at low temperatures, while a stronger interaction (Au with Ti-O-Si species) leads to reduction at higher temperatures [52].

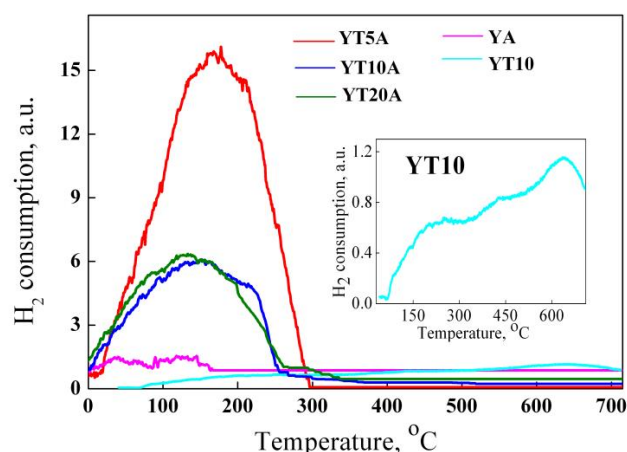


**Figure 12.** H<sub>2</sub>-TPR profiles of the obtained samples.

The shift to lower temperature can be seen for both the YT20A sample (Figure 12). More significant shoulders of YT20A and YT10A reduction profiles can be assigned to the adsorption of hydrogen (the first) and hydrogen spillover (the second). In fact, metallic gold plays an important role in hydrogen spillover and thus reactive atomic hydrogen can directly diffuse over the solid surface and react with titanium oxide [53]. Furthermore, the hydrogen migration over non-reducible supports such as zeolites [54] is mediated by H-species which interact in particular with defect sites of this [55]. So, the defects' abundance of support enhances the hydrogen diffusion and spillover phenomenon depending on their availability. The surface vacancies are the effect of titania loading, dispersion, and interaction with the surface of zeolite support. Regarding titanium species reduction, no characteristic peak was evidenced for all the samples, probably due to the high dispersion of these species, their high interaction with porous support, and the protective effect of gold nanoparticles, as it was suggested in a previous study [56].

### 2.2.9. CO<sub>2</sub>-TPD Results

The CO<sub>2</sub>-temperature programmed desorption (TPD) profiles recorded for the samples showed a similar temperature (around 180 °C) of CO<sub>2</sub> desorption peak for YT20A and YT5A samples (Figure 13) and a shift to a slightly lower temperature (150 °C) for YT10A sample. The peaks recorded in the thermal desorption spectrum are attributed to different bonds of CO<sub>2</sub> to the regular sites on the surface. Desorption profiles show one peak for all the samples based on zeolite Y, indicating one kind of CO<sub>2</sub> interaction (weak for YT10A, weak-moderate for YT5A and YT20A samples).

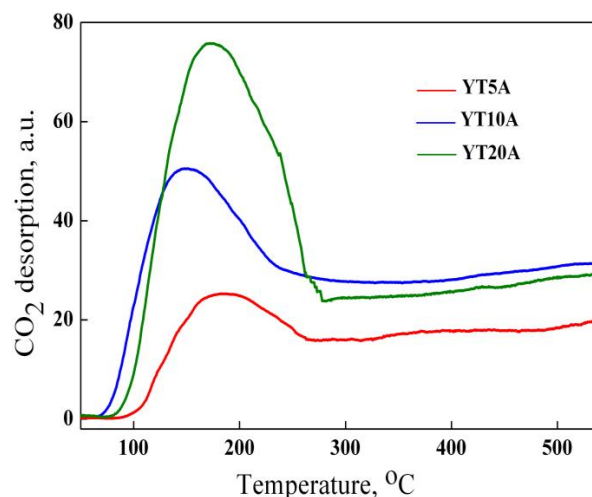


**Figure 13.** CO<sub>2</sub>-TPD profiles of the studied materials.

CO<sub>2</sub>-TPD results reflect also the increase in CO<sub>2</sub> adsorption with titania loading. Therefore, the amount of TiO<sub>2</sub> influences the number of sites, but also their strength. A different number of oxygen vacancies could be created by the immobilization of TiO<sub>2</sub> on zeolite Y, as a result of the interaction between TiO<sub>2</sub> and support. The electron pair remained in the vacancy after oxygen defect formation at the interface of TiO<sub>2</sub> and SiO<sub>2</sub> moved toward the neighboring Ti atoms [57].

#### 2.2.10. Adsorption Studies

It is well known that adsorption is an effective method for removing several pollutants from wastewater [58]. On the other hand, in photocatalytic degradation of organic molecules from wastewater, adsorption, and photocatalytic reactions occur simultaneously and have a synergistic effect on efficiency [59]. It was previously reported [20] for the case of the YT10A sample that in the first 3 h, the variation of AMX concentration in solution is strongly influenced by adsorption. After this period of time, the significant decrease in AMX concentration can be attributed to the photocatalytic process. In the photocatalytic degradation of AMX, adsorption can be considered a rate-determining step [47].

The adsorption studies of AMX on the photocatalysts was evaluated in dark conditions. The obtained results are presented in Figure 14.

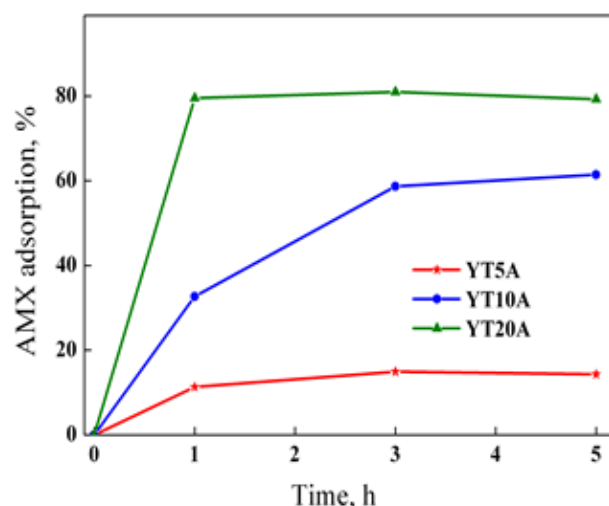
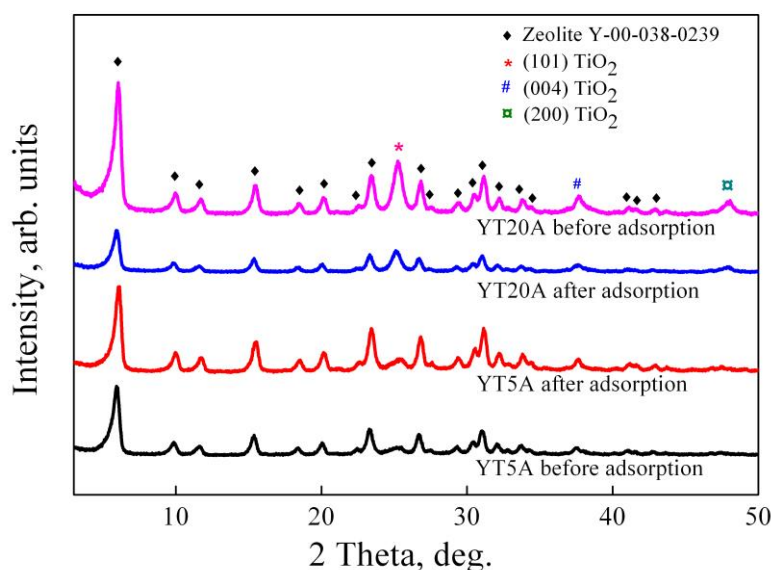


Figure 14. AMX adsorption capacity of the prepared materials.

Figure 14 revealed a significant increase in AMX adsorption in the first hour. After that, the variation is insignificant, tending to a level reached after three hours for all samples. The adsorption capacity increased with titania content, such as the best results were obtained for the YT20A sample. It is observed that the maximum and minimum adsorption capacities were obtained for samples with the highest and lowest TiO<sub>2</sub> loading. The increase in adsorption with TiO<sub>2</sub> loading was attributed to the created defect sites that enhanced the surface basicity, as was demonstrated by CO<sub>2</sub>-TPD results (Figure 13). Furthermore, it seems that the weak-moderate character of the basic sites in the case of samples YT10A and YT20A favors the adsorption capacity of weakly acidic amoxicillin molecules.

The synthesized samples show a high stability, as was suggested by XRD measurements (Figure 15) which indicated the same pattern of materials before and after adsorption process. However, in the case of YT20A sample, a considerable decrease in the intensity of diffraction peaks was found. This result may be associated with the decrease in crystallinity and may be due to the presence of amoxicillin molecules in a larger amount on the zeolitic structure of the photocatalyst [60]. The results presented in Figure 14 indicate the highest adsorption capacity for this sample.



**Figure 15.** Wide-angle X-ray diffraction patterns of the samples before and after adsorption of amoxicillin.

#### 2.2.11. Photocatalytic Activity

The degradation of AMX under UV and visible light irradiation ( $\lambda = 254$  nm and  $\lambda = 532$  nm) using the obtained photocatalysts showed the effect of  $\text{TiO}_2$  loading on the process efficiency. The obtained results are shown in Figure 16a,b.

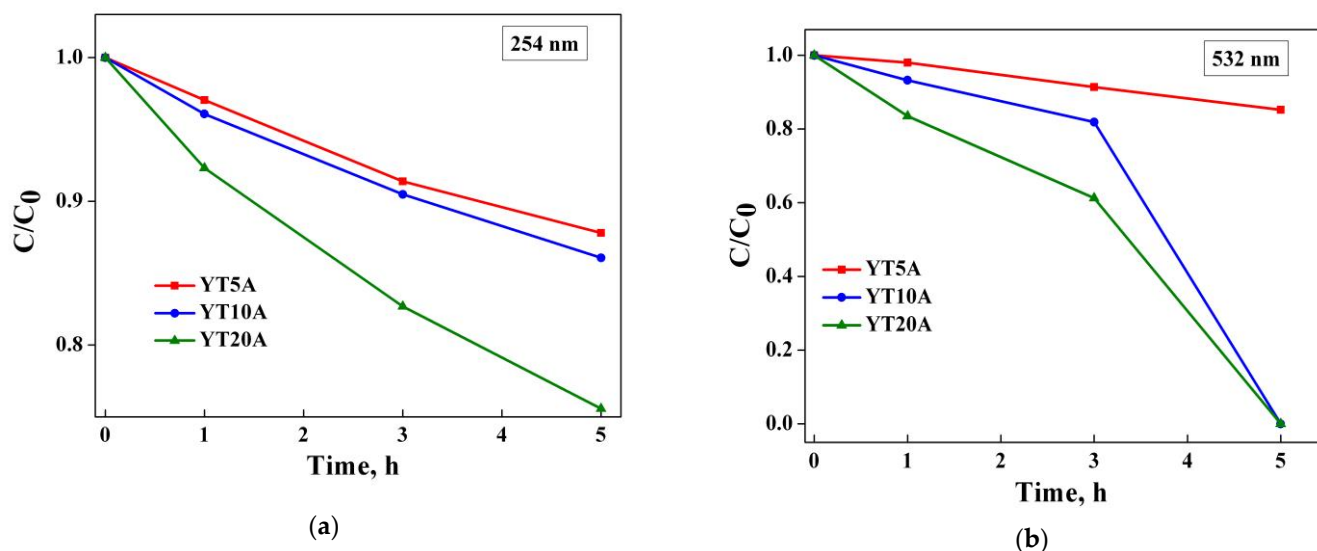


**Figure 16.** Photocatalytic degradation of amoxicillin under UV (a) and visible light irradiation (b) using the Au–Ti materials.

It has shown a direct dependence between the photocatalytic process and adsorption capacity (Figure 14), highlighting the importance of providing pollutant molecules on the surface of the photocatalytic material, close to the activated sites under irradiation [47]. Thus, the photocatalytic properties of the synthesized materials increased with the  $\text{TiO}_2$  loading, both under UV and visible light irradiation.

It is worth discussing the exceptional results obtained in the case of samples with 10 and 20%  $\text{TiO}_2$  under visible light irradiation. As can be seen from Figure 16b, the total degradation of amoxicillin was achieved after 5 h of irradiation. This behavior can be explained by the presence of metallic gold nanoparticles Au NPs and additionally, gold nanoclusters Au NCs (see Table 2) which act as  $e^-$  donors under visible light irradiation.

Both Au NPs and Au NCs have a key role in the photocatalytic performance of the synthesized materials, but each act differently. Thus, under the effect of visible irradiation, Au NPs exhibit surface plasmonic effect leading to the generation of hot electrons that are injected directly into the conduction band of TiO<sub>2</sub>. In addition to this aspect, the Schottky barrier that forms at the interface between the metallic gold nanoparticles and TiO<sub>2</sub> prevents the return of the injected electrons, leading to a better separation of the e<sup>-</sup>/h<sup>+</sup> species, which is desirable in photocatalysis [61]. In the case of photoactivated Au NCs, known as having abundant unsaturated active sites [62], there is a discrete e<sup>-</sup> transition from the LUMO to HOMO energy levels and further, to the conduction band of TiO<sub>2</sub> [61].

In the case of UV light irradiation, when only TiO<sub>2</sub> is activated, the metallic gold species act as e<sup>-</sup> trappers which would imply an improvement of the photocatalytic activity due to the separation of charge carriers [20,61]. However, the photocatalytic performances obtained are lower than in the case of visible irradiation (Figure 16). The same behavior is also discussed in other studies reported in the literature [63] and is attributed to the low capacity of Au NCs to accept electrons photogenerated by TiO<sub>2</sub> [64] and to their low bandgap (1.3–1.4 eV) that allows activation only under visible irradiation [65,66].

### 2.2.12. Kinetic Studies

The photocatalytic degradation of amoxicillin by Ti–Au synthesized materials was studied using a pseudo-first-order kinetic model, expressed as  $\ln(C_0/C) = k_{app}t$ . The kinetics results obtained under UV and visible light irradiation are presented in Figure 17a,b.

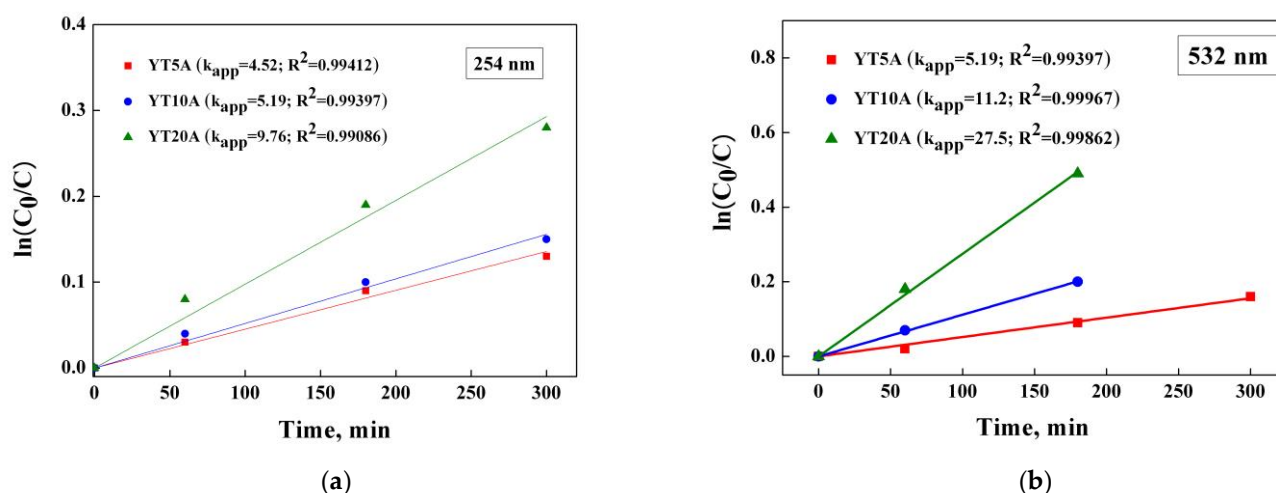


**Figure 17.** Kinetic and apparent rate constant  $k_{app}$  values ( $\times 10^{-4} \text{ min}^{-1}$ ) of AMX photocatalytic degradation under UV (a) and visible light irradiation (b).

The high values of linear regression coefficients ( $R^2$ ) obtained for the kinetic plots for all the synthesized materials confirm the pseudo-first-order type of photocatalytic reactions, as was previously reported [67]. The calculated values of the apparent rate constant ( $k_{app}$ ) are exposed in Figure 17. It can be seen the increasing of  $k_{app}$  values with titania content. The effect is more significant under visible light due to the surface plasmon resonance (SPR) effect of gold in interaction with supported titania [68].

### 2.2.13. Toxicity Assessment

Toxicity assessment, before and after photocatalytic reactions, was conducted to evaluate the amoxicillin degradation and formation of non-toxic intermediates in terms of antimicrobial effect. The results are exposed in Figure 18 and show a decrease in inhibition percentage compared to the initial amoxicillin solution. Furthermore, it can be observed that irradiation conditions influence the nature of AMX degradation products and consequently, their toxicity. The toxicity results highlight the lowest residual toxicity under UV

irradiation and a higher one in the case of visible light conditions. These results may be the effect of different reaction mechanisms for these photocatalysts under UV or visible light.

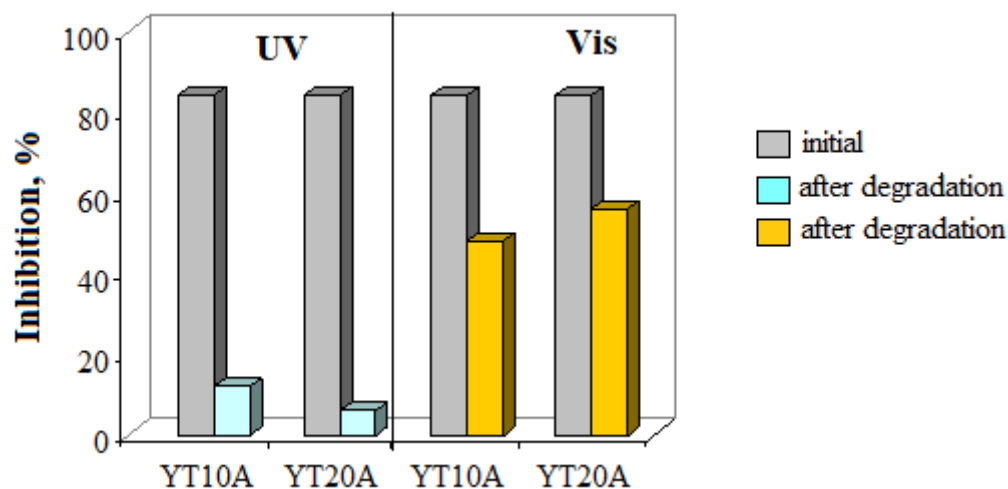


**Figure 18.** Changes in bacterial (*S. aureus*) inhibition of AMX solution after photocatalytic reactions under UV and visible light irradiation.

### 3. Conclusions

High-performance photocatalysts were synthesized by the processing of aluminosilicate gel in order to obtain zeolite Y with a very well-organized structure and further, modified with TiO<sub>2</sub> and gold species by impregnation. Aging of aluminosilicate gel in static conditions and mixing the precursors required for the synthesis gel under magnetic stirring leads to the obtaining of highly crystallized zeolite Y with homogeneous morphology, desirable properties in tailoring high-performance photocatalysts. Different TiO<sub>2</sub> loadings were used (5, 10, 20%), and was studied their interaction with the subsequently immobilized gold species. The main important changes that appeared in the structural, textural, morphological, and optical properties of materials were discussed. An increase in anatase crystallite size was noticed with TiO<sub>2</sub> loading and a different reducing capacity of Au<sup>3+</sup> species. XPS results showed the production of only metallic gold nanoparticles for the YT5A sample, while for the YT10A and YT20A samples, intermediate gold states of the Au<sup>+1</sup> type, as well as clusters, were also obtained. PL spectroscopy showed that a larger amount of TiO<sub>2</sub> led to a delay in the recombination capacity of the photogenerated electron–hole pairs, which is desirable in photocatalysis. Additionally, an improvement in the adsorption capacity of the organic pollutant (amoxicillin) was obtained by increasing the amount of TiO<sub>2</sub>, due to the high number of basic sites on the surface of the material. All these properties are responsible for the photocatalytic results obtained in the degradation of amoxicillin. Thus, the best performances were obtained for the YT20A sample with 20% TiO<sub>2</sub>, achieving a total degradation of amoxicillin under visible irradiation after 5 h. The plasmonic effect of gold nanoparticles also has a contributing role in the case of visible light irradiation. It was demonstrated that the materials synthesized in the present work have the ability to turn amoxicillin into products with much lower toxicity, both in UV and visible light.

### 4. Materials and Methods

#### 4.1. Materials

##### 4.1.1. Chemicals

To obtain the aluminosilicate gel, we used sodium silicate solution (26.5 wt.% SiO<sub>2</sub>, 10.6 wt. % Na<sub>2</sub>O, Sigma Aldrich, Darmstadt, Germany) and sodium aluminate (NaAlO<sub>2</sub>, Sigma Aldrich) as silica and alumina sources, respectively. To provide the strong basic medium necessary for assembling structural units of zeolite Y, NaOH (98 wt.%, Lach-Ne) was chosen. Titanium (IV) n-butoxide (99%, Acros Organics, Geel, Belgium) and gold

chloride ( $\text{HAuCl}_4\text{aq}$ , purum 51.5% Au brown, Fluka, Buchs, Switzerland) were used as precursors for the modification of zeolite Y with  $\text{TiO}_2$  and Au species, respectively.

#### 4.1.2. Sample Preparation

The synthesis of zeolite Y was used as support for obtaining the photocatalytic materials and was carried out by a hydrothermal method in two steps that involves the use of seed gel obtained first [34]. In the second step, aluminosilicate gel with the final molar ratio  $0.66\text{Na}_2\text{O}:0.21\text{Al}_2\text{O}_3:\text{SiO}_2:19.1\text{H}_2\text{O}$ , was prepared and the resulting seed gel was added. This mixture was aged for 24 h at room temperature and further, 6 h at  $100^\circ\text{C}$  in a Teflon-lined autoclave. The formation of the aluminosilicate gel and its evolution during the zeolitization process was described in detail in a study recently reported by our group [30]. In order to obtain the aluminosilicate support with suitable properties for photocatalysis, the treatment of the corresponding gel resulting from mixing sodium silicate with sodium aluminate was completed differently. As suggested in Figure 19, the method of mixing the precursors (stirring vs sonication), and the presence or absence of agitation during the aging of aluminosilicate hydrogel were varied. The zeolite powders thus obtained were denoted Yag, Y, and Yus.

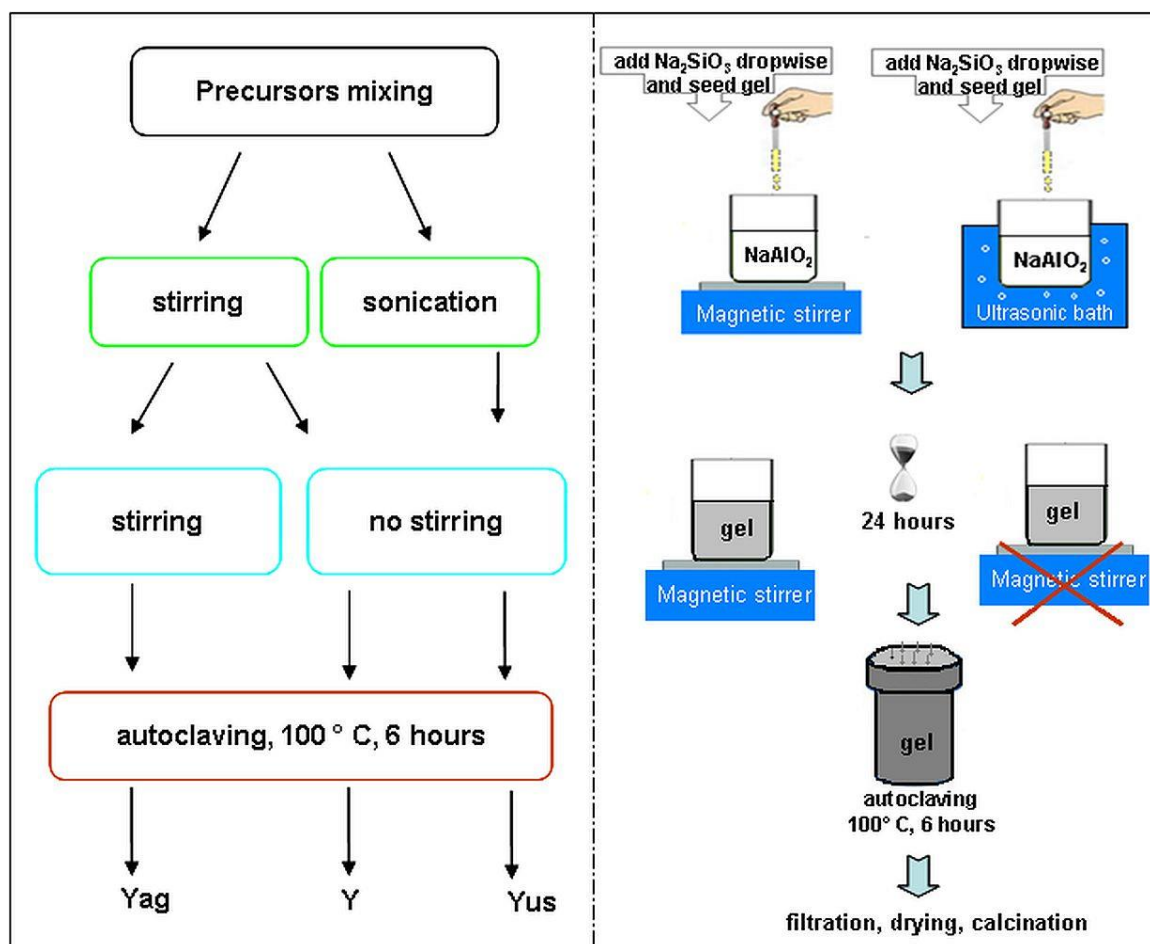


**Figure 19.** Schematic representation of the various treatments of aluminosilicate gel during the synthesis of faujasite Y.

Further,  $\text{TiO}_2$  and Au were immobilized on zeolite Y powder obtained by the second route (according to Figure 19) by impregnation method using the corresponding precursor. Firstly,  $\text{TiO}_2$  was supported on zeolite in different concentrations (5 wt.%, 10 wt.%, 20 wt.%) from an alcoholic solution of titanium (IV) n-butoxide. To eliminate traces of organics from the precursor, the samples were calcined in air at  $600^\circ\text{C}$  for 8 h. Secondly, 1 wt.% gold

was added on Ti-modified zeolite Y from an aqueous solution of  $\text{HAuCl}_4$ . Chlorine was removed by washing with  $\text{Na}_2\text{CO}_3$ . Finally, the samples were washed with deionized water, dried at room temperature until the next day, and further at  $120\text{ }^\circ\text{C}$  for 6 h. The materials thus synthesized were labeled YT5A, YT10A, and YT20A.

#### 4.2. Methods of Characterization

Wide-angle X-ray diffraction (XRD) patterns of the samples were recorded using a Rigaku Ultima IV diffractometer (Rigaku Corp., Tokyo, Japan) with  $\text{Cu K}\alpha$  ( $\lambda = 0.15406\text{ nm}$ ).  $\text{TiO}_2$  crystallite size was calculated according to Scherrer's formula:  $D = k \cdot \lambda / (\text{FWHM}) \cdot \cos(\theta)$  along the (101) direction, where  $\lambda$  = wavelength of the  $\text{Cu K}\alpha$  radiation ( $1.54056\text{ \AA}$ ), FWHM = full width at half maximum of the intensity vs.  $2\theta$  profile,  $\theta$  = Bragg's diffraction angle and  $k = 0.9$  (shape factor).

$\text{N}_2$  physisorption analysis was performed for textural characterization of the samples using a Micromeritics ASAP 2020 analyzer (Norcross, GA, USA).

Morphological investigations of zeolite Y before and after modification with Ti and Au active species were performed by means of a scanning electron microscope (ZEISS EVO LS10 SEM, Oberkochen, Germany).

X-ray photoelectron spectroscopy was used to analyze the main species on the surface of the materials using an XPS—PHI Quantera equipment (Ontario, ON, Canada) with a monochromatized  $\text{Al K}\alpha$  radiation ( $1486.6\text{ eV}$ ). The overall energy resolution was estimated at  $0.6\text{ eV}$  by the full width at half-maximum (FWHM) of the  $\text{Au}4f_{7/2}$  photoelectron line ( $84\text{ eV}$ ).

UV–Raman spectra of the samples were recorded by means of a LabRam HR800 spectrometer (Horiba France SAS, Palaiseau, France). Catalysts were excited with a  $325\text{ nm}$  line through an  $\times 40/0.47\text{ NUV}$  objective from Olympus Corporation, Tokyo, Japan. The experimental setup (UV laser and rejection filter) prevented recording Raman spectra at lower wavenumbers.

The UV–Vis diffuse reflectance spectra of the photocatalysts were recorded in the range of  $200\text{--}700\text{ nm}$  using a JASCO V570 spectrophotometer (Tokyo, Japan).

An FLSP 920 spectrofluorimeter (Edinburgh Instruments, Livingston, UK) with a Xe lamp as an excitation source ( $\lambda_{\text{exc}} = 550\text{ nm}$ ) was used to record the photoluminescence spectra of the samples between  $570$  and  $800\text{ nm}$ . The excitation and emission slits were  $10\text{ nm}$  for all measurements.

For the temperature-programmed reduction of the samples by hydrogen ( $\text{H}_2$ -TPR), a ChemBET 3000-Quantachrome (Boynton Beach, FL, USA) coupled with a thermal conductivity detector (TCD) was used. The experiments were carried out in a flow system using Ar ( $70\text{ mL/min}$ ) and  $5\%$  volume  $\text{H}_2$  over  $50\text{ mg}$  photocatalyst.  $\text{H}_2$ -TPR profiles were recorded up to  $850\text{ }^\circ\text{C}$ , with a heating rate of  $10\text{ }^\circ\text{C/min}$ . A silica gel column was used for the optimal operation of the thermal conductivity detector.

The adsorption properties for  $\text{CO}_2$  were measured by TPD of  $\text{CO}_2$  with a Quantachrome ChemBET 3000 apparatus (USA) equipped with a thermal conductivity detector (TCD). Before adsorption, the samples ( $50\text{ mg}$ ) were pretreated with a helium flux from room temperature up to  $300\text{ }^\circ\text{C}$  and kept for 1 h (heating rate of  $10\text{ }^\circ\text{C/min}$ ). Then, the samples were cooled at  $100\text{ }^\circ\text{C}$  and saturated with a  $\text{CO}_2$  stream ( $30\text{ mL/min}$ ). After baseline stabilization, the temperature of the reactor was increased by  $10\text{ }^\circ\text{C/min}$  until all the  $\text{CO}_2$  was desorbed. Desorbed  $\text{CO}_2$  amounts were calculated from the area of the obtained peaks.

The adsorption and photocatalytic experiments were carried out under stirring in a dark room at a constant temperature of  $30\text{ }^\circ\text{C}$  by adding  $20\text{ mg}$  of the photocatalyst  $10\text{ mL}$  aqueous solution of amoxicillin, AMX ( $30\text{ mg/L}$ ). For the photocatalytic tests, a halogen lamp ( $2 \times 60\text{ W}$ ) was used with a filter for  $\lambda = 254\text{ nm}$  and a DPSS-532-100 laser (Apel Laser, Bucharest, Romania) for visible light ( $\lambda = 532\text{ nm}$ ). The UV or visible light irradiation was started after stirring the reaction mixture for  $30\text{ min}$  in the dark in order to allow the AMX adsorption on the photocatalysts' surface. At given intervals of time (1, 3,

and 5 h of irradiation), 3 mL of suspension was taken out and filtered using a Millipore syringe filter of 0.45  $\mu\text{m}$  in order to remove the photocatalyst from the suspension. Further, the filtered solution was spectrophotometrically analyzed by means of the same JASCO V570 UV–Vis spectrophotometer, reading the maximum absorbance of AMX molecules ( $\lambda = 230$  nm). Finally, the evaluation of AMX degradation was expressed as  $C/C_0$ , where  $C$  is the concentration of the solution taken out at time  $t$  (1, 3, or 5 h) and  $C_0$  is the initial concentration, at  $t = 0$ . The relation  $\ln(C/C_0) = k_{\text{app}}t$  was used to obtain the apparent rate constant ( $k_{\text{app}}$ ), considering that the AMX degradation process is a first-order reaction.

Toxicity assessment, before and after photocatalytic reactions, was conducted to evaluate the amoxicillin degradation and formation of non-toxic intermediates in terms of antimicrobial effect. For this purpose, the antibacterial activity was performed by diffusiometric method using disk and spot inoculation on agar Mueller Hinton medium (Scharlau, Spain) with the composition (g/L: 17.5, peptone; 1.5, starch; 2.0, meat infusion solids). Bacterial suspension of *Staphylococcus aureus* (with concentration of  $1-3 \times 10^8$  CFU/mL) was used to inoculate the agar media, followed by the application of a volume of 10  $\mu\text{L}$  of the tested solution. Subsequently, plates were incubated for 24 h at 35  $^\circ\text{C}$ . The antibacterial effect was evaluated by observing the presence and measuring the clear halo developed around the inoculation area.

**Author Contributions:** Conceptualization, V.P.; methodology, V.P. and G.P.; validation, V.P.; formal analysis, G.P.; investigation, G.P., F.P., I.A., S.P., E.M.A. and S.S.; data curation, G.P., F.P., I.A., S.P., E.M.A., S.S., D.C.C., A.B., E.M.C., L.M.J. and M.C.; writing—original draft preparation, G.P., E.M.A., S.S. and V.P.; writing—review and editing, V.P. and G.P.; visualization, V.P. and G.P.; supervision, V.P. All authors have read and agreed to the published version of the manuscript.

**Funding:** This research received no external funding.

**Institutional Review Board Statement:** Not applicable.

**Informed Consent Statement:** Not applicable.

**Data Availability Statement:** The data presented in this study are available on request from the corresponding author.

**Acknowledgments:** The authors would like to thank Alin Enache (Apel Laser) for the visible light laser (DPSS-532-100,  $\lambda = 532$  nm) used for the photocatalytic experiments and PN 23.06 Core Program—ChemNewDeal within the National Plan for Research, Development and Innovation 2022-2027, developed with the support of Ministry of Research, Innovation, and Digitization, project no. PN 23.06.01.01-AQUAMAT, for the microbiological analysis.

**Conflicts of Interest:** The authors declare no conflict of interest.

## References

1. Kornas, A.; Olszówka, J.E.; Urbanova, M.; Brabec, L.; Rathousky, J.; Dedecek, J.; Pashkova, V. Ultrasonic Pretreatment as a Tool for the Preparation of Low-Defect Zeolite Mordenite. *ACS Omega*. **2021**, *6*, 2340–2345. [[CrossRef](#)] [[PubMed](#)]
2. Hamidi, F.; Bengueddach, A.; Di Renzo, F.; Fajula, F. Control of Crystal Size and Morphology of Mordenite. *Catal. Lett.* **2003**, *87*, 149–152. [[CrossRef](#)]
3. Li, S.; Li, J.; Dong, M.; Fan, S.; Zhao, T.; Wang, J.; Fan, W. Strategies to control zeolite particle morphology. *Chem. Soc. Rev.* **2019**, *48*, 885–907. [[CrossRef](#)] [[PubMed](#)]
4. Lutz, W. Zeolite Y: Synthesis, Modification, and Properties—A Case Revisited. *Adv. Mater. Sci. Eng.* **2014**, *2014*, 724248. [[CrossRef](#)]
5. Yu, J. Synthesis of zeolites. In *Introduction to Zeolite Science and Practice*, 3rd ed.; Cejka, J., van Bekkum, H., Corma, A., Schuth, F., Eds.; Elsevier: Amsterdam, The Netherlands, 2007; Volume 168, pp. 40–103.
6. Munguti, L.K.; Dejene, F.B.; Muthee, D.K. Zeolite Na-A supported TiO<sub>2</sub>: Effects of TiO<sub>2</sub> loading on structural, optical and adsorption properties. *Mater. Sci. Eng. B* **2023**, *289*, 116281. [[CrossRef](#)]
7. Fernández-Catalá, J.; Sánchez-Rubio, M.; Navlani-García, M.; Berenguer-Murcia, A.; Cazorla-Amorós, D. Synthesis of TiO<sub>2</sub>/Nanozeolite Composites for Highly Efficient Photocatalytic Oxidation of Propene in the Gas Phase. *ACS Omega* **2020**, *5*, 31323–31331. [[CrossRef](#)]
8. Joseph, C.G.; Sharain-Liew, Y.L.; Bono, A.; Teng, L.Y. Photodegradation of Indigo Dye Using TiO<sub>2</sub> and TiO<sub>2</sub>/Zeolite System. *Asian J. Chem.* **2013**, *25*, 8402–8406. [[CrossRef](#)]

9. Xie, Y.; Wang, J.; Ren, F.; Shuai, H.; Du, G. Nonmetallic Mineral as the Carrier of TiO<sub>2</sub> Photocatalyst: A Review. *Front. Catal.* **2022**, *2*, 806316. [[CrossRef](#)]
10. Yang, H.; Yang, B.; Chen, W.; Yang, J. Preparation and Photocatalytic Activities of TiO<sub>2</sub>-Based Composite Catalysts. *Catalysts* **2022**, *12*, 1263. [[CrossRef](#)]
11. Dong, H.; Zeng, G.; Tang, L.; Fan, C.; Chang Zhang, C.; He, X.; He, Y. An overview on limitations of TiO<sub>2</sub>-based particles for photocatalytic degradation of organic pollutants and the corresponding countermeasures. *Water Res.* **2015**, *79*, 128–146. [[CrossRef](#)]
12. Awad, M.E.; Farrag, A.M.; El-Bindary, A.A.; El-Bindary, M.A.; Kiwaan, H.A. Photocatalytic degradation of Rhodamine B dye using lowcost pyrofabricated titanium dioxide quantum dotskaolinite nanocomposite. *Appl. Organomet. Chem.* **2023**, e7113. [[CrossRef](#)]
13. Preda, S.; Pandele-Cusu, J.; Petrescu, S.V.; Ciobanu, E.M.; Petcu, G.; Culita, D.C.; Apostol, N.G.; Costescu, R.M.; Raut, I.; Constantin, M.; et al. Photocatalytic and Antibacterial Properties of Doped TiO<sub>2</sub> Nanopowders Synthesized by Sol–Gel Method. *Gels* **2022**, *8*, 673. [[CrossRef](#)]
14. Predoana, L.; Petcu, G.; Preda, S.; Pandele-Cus, U.J.; Petrescu, S.V.; Baran, A.; Apostol, N.G.; Costescu, R.M.; Surdu, V.-A.; Vasile, B.Ş.; et al. Copper-/Zinc-Doped TiO<sub>2</sub> Nanopowders Synthesized by Microwave-Assisted Sol–Gel Method. *Gels* **2023**, *9*, 267. [[CrossRef](#)]
15. Jaybhaye, S.; Shinde, N.; Jaybhaye, S.; Narayan, H. Photocatalytic Degradation of Organic Dyes Using Titanium Dioxide (TiO<sub>2</sub>) and Mg-TiO<sub>2</sub> Nanoparticles. *J. Nanotechnol. Nanomater.* **2022**, *3*, 67–76. [[CrossRef](#)]
16. Predoană, L.; Ciobanu, E.M.; Petcu, G.; Preda, S.; Pandele-Cuşu, J.; Anghel, E.M.; Petrescu, S.V.; Culiță, D.C.; Băran, A.; Surdu, V.-A.; et al. Photocatalytic Performance of Sn-Doped TiO<sub>2</sub> Nanopowders for Photocatalytic Degradation of Methyl Orange Dye. *Catalysts* **2023**, *13*, 534. [[CrossRef](#)]
17. Usman, A.K.; Cursaru, D.-L.; Branoiu, G.; Somoghi, R.; Manta, A.-M.; Matei, D.; Mihai, S. A Modified Sol–Gel Synthesis of Anatase {001}-TiO<sub>2</sub>/Au Hybrid Nanocomposites for Enhanced Photodegradation of Organic Contaminants. *Gels* **2022**, *8*, 728. [[CrossRef](#)]
18. Park, B.-G. Photocatalytic Activity of TiO<sub>2</sub> -Doped Fe, Ag, and Ni with N under Visible Light Irradiation. *Gels* **2022**, *8*, 14. [[CrossRef](#)]
19. Khusnun, N.F.; Jalil, A.A.; Abdullah, T.A.T.; Latip, S.S.M.; Hitam, C.N.C.; Fauzi, A.A.; Hassan, N.S.; Aziz, M.A.H.; Rahman, A.F.A.; Aziz, F.F.A.; et al. Influence of TiO<sub>2</sub> dispersion on silica support toward enhanced amine assisted CO<sub>2</sub> photoconversion to methanol. *J. CO<sub>2</sub> Util.* **2022**, *58*, 101901. [[CrossRef](#)]
20. Petcu, G.; Anghel, E.M.; Buixaderas, E.; Atkinson, I.; Somacescu, S.; Baran, A.; Culita, D.C.; Trica, B.; Bradu, C.; Ciobanu, M.; et al. Au/Ti Synergistically Modified Supports Based on SiO<sub>2</sub> with Different Pore Geometries and Architectures. *Catalysts* **2022**, *12*, 1129. [[CrossRef](#)]
21. Danfá, S.; Oliveira, C.; Santos, R.; Martins, R.C.; Quina, M.M.J.; Gomes, J. Development of TiO<sub>2</sub>-Based Photocatalyst Supported on Ceramic Materials for Oxidation of Organic Pollutants in Liquid Phase. *Appl. Sci.* **2022**, *12*, 7941. [[CrossRef](#)]
22. Hadjltaief, H.B.; Omri, A.; Zina, B.B.; Da Costa, P.; Galvez, M.E. Titanium Dioxide Supported on Different Porous Materials as Photocatalyst for the Degradation of Methyl Green in Wastewaters. *Adv. Mater. Sci. Eng.* **2015**, *2015*, 759853. [[CrossRef](#)]
23. Kucerová, G.; Strunk, J.; Muhler, M.; Behm, R.J. Effect of titania surface modification of mesoporous silica SBA-15 supported Au catalysts: Activity and stability in the CO oxidation reaction. *J. Catal.* **2017**, *356*, 214–228. [[CrossRef](#)]
24. Liao, G.; He, W.; He, Y. Investigation of Microstructure and Photocatalytic Performance of a Modified Zeolite Supported Nanocrystal TiO<sub>2</sub> Composite. *Catalysts* **2019**, *9*, 502. [[CrossRef](#)]
25. Ayati, A.; Ahmadpour, A.; Bamoharram, F.F.; Tanhaei, B.; Manttari, M.; Sillanpaa, M. A review on catalytic applications of Au/TiO<sub>2</sub> nanoparticles in the removal of water pollutant. *Chemosphere* **2014**, *107*, 163–174. [[CrossRef](#)]
26. Yu, H.; Li, S.; Peng, S.; Yu, Z.; Chen, F.; Liu, X.; Guo, J.; Zhu, B.; Huang, W.; Zhang, S. Construction of rutile/anatase TiO<sub>2</sub> homojunction and metal-support interaction in Au/TiO<sub>2</sub> for visible photocatalytic water splitting and degradation of methylene blue. *Int. J. Hydrog. Energ.* **2023**, *48*, 975–990. [[CrossRef](#)]
27. Zerjav, G.; Roskari, M.; Zavasnik, J.; Kovac, J.; Pintar, A. Effect of Au loading on Schottky barrier height in TiO<sub>2</sub> + Au plasmonic photocatalysts. *Appl. Surf. Sci.* **2022**, *579*, 152196. [[CrossRef](#)]
28. Li, X.; Luo, Y.; Wu, S.; Lian, H.; Deng, X. The exceptional performance of the plasmonic Au-Fe/TiO<sub>2</sub> nanocatalysts achieved by O<sub>2</sub> plasma activation. *Catal. Today* **2023**, *418*, 114106. [[CrossRef](#)]
29. Sun, Z.-G.; Li, X.-S.; Liu, J.-L.; Li, Y.-C.; Zhu, B.; Zhu, A.-M. A promising visible-light photocatalyst: H<sub>2</sub> plasma-activated amorphous-TiO<sub>2</sub>-supported Au nanoparticles. *J. Catal.* **2019**, *375*, 380–388. [[CrossRef](#)]
30. Petcu, G.; Dobrescu, G.; Atkinson, I.; Ciobanu, M.; Blin, J.-L.; Parvulescu, V. Evolution of Morphology, Fractal Dimensions, and Structure of (Titanium) Aluminosilicate Gel during Synthesis of Zeolites Y and Ti-Y. *Fractal Fract.* **2022**, *6*, 663. [[CrossRef](#)]
31. Treacy, M.M.J.; Higgins, J.B. *Collection of Simulated XRD Powder Patterns for Zeolites*, 4th ed.; Elsevier: Amsterdam, The Netherlands, 2001; pp. 154–155.
32. Yu, Y.; Xiong, G.; Li, C.; Xiao, F.S. Characterization of aluminosilicate zeolites by UV Raman spectroscopy. *Micropor. Mesopor. Mater.* **2001**, *46*, 23–34. [[CrossRef](#)]
33. Kishor, R.; Singh, S.B.; Ghoshal, A.K. Role of metal type on mesoporous KIT-6 for hydrogen storage. *Int. J. Hydrog. Energ.* **2018**, *43*, 10376–10385. [[CrossRef](#)]

34. Petcu, G.; Anghel, E.M.; Somacescu, S.; Preda, S.; Culita, D.; Mocanu, S.; Ciobanu, M.; Parvulescu, V. Hierarchical Zeolite Y Containing Ti and Fe Oxides as Photocatalysts for Degradation of Amoxicillin. *J. Nanosci. Nanotechnol.* **2020**, *20*, 1158–1169. [[CrossRef](#)]
35. Lopez-Tenllado, F.J.; Estevez, R.; Hidalgo-Carrillo, J.; Lopez-Fernandez, S.; Urbano, F.J.; Marinas, A. Hydrogen photo-production from glycerol on platinum, gold and silver-modified TiO<sub>2</sub>-USY62 catalysts. *Catal. Today* **2022**, *390–391*, 92–98. [[CrossRef](#)]
36. Naumkin, A.V.; Kraut-Vass, A.; Gaarenstroom, S.W.; Poell, C.J. *NIST X-Ray Photoelectron Spectroscopy Database*, Version 4.1. NIST Standard Reference Database NIST SRD 20. National Institute of Standards and Technology: Gaithersburg, MD, USA, 2012.
37. Moulder, F.; Stickle, W.F.; Sobol, P.E.; Bomben, K.D. *Handbook of X-Ray Photoelectron Spectroscopy*; ULVAC-PHI, Inc.: Chigasaki, Japan; Perkin-Elmer Corporation: Eden Prairie, MN, USA, 1995; p. 370.
38. Petcu, G. Performing Catalytic Materials Based on Zeolite Y and Mesoporous Silica, Functionalized with Transition Metals, Used in Degradation and Recovery of Different Pollutants from Water and Air. Ph.D. Thesis, School of Advanced Studies of the Romanian Academy, Bucharest, Romania, 26 October 2021.
39. Perera, A.S.; Trogadas, P.; Nigra, M.M.; Yu, H.; Coppens, M.O. Optimization of mesoporous titanosilicate catalysts for cyclohexene epoxidation via statistically guided synthesis. *J. Mater. Sci.* **2018**, *53*, 7279–7293. [[CrossRef](#)]
40. Hess, C. New advances in using Raman spectroscopy for the characterization of catalysts and catalytic reactions. *Chem. Soc. Rev.* **2021**, *50*, 3519. [[CrossRef](#)]
41. Zhang, J.; Xu, Q.; Li, M.; Feng, Z.; Li, C. UV Raman Spectroscopic Study on TiO<sub>2</sub>. II. Effect of Nanoparticle Size on the Outer/Inner Phase Transformations. *J. Phys. Chem. C* **2009**, *113*, 1698–1704. [[CrossRef](#)]
42. Peng, R.; Zhao, D.; Dimitrijevic, N.M.; Rajh, T.; Koodali, R.T. Room Temperature Synthesis of Ti–MCM-48 and Ti–MCM-41 Mesoporous Materials and Their Performance on Photocatalytic Splitting of Water. *J. Phys. Chem. C* **2012**, *116*, 1605–1613. [[CrossRef](#)]
43. Sacaliuc, E.; Beale, A.M.; Weckhuysen, B.M.; Nijhuis, T.A. Propene epoxidation over Au/Ti-SBA-15 catalysts. *J. Catal.* **2007**, *248*, 235–248. [[CrossRef](#)]
44. Jianga, C.; Lee, K.Y.; Parlett, C.M.A.; Bayazit, M.K.; Lau, C.C.; Ruan, Q.; Moniz, S.J.A.; Lee, A.F.; Tang, J. Size-controlled TiO<sub>2</sub> nanoparticles on porous hosts for enhanced photocatalytic hydrogen production. *Appl. Catal. A Gen.* **2016**, *521*, 133–139. [[CrossRef](#)]
45. Yadav, R.; Amoli, V.; Singh, J.; Tripathi, M.K.; Bhanja, P.; Bhaumik, A.; Sinha, A.K. Plasmonic gold deposited on mesoporous Ti<sub>x</sub>Si<sub>1-x</sub>O<sub>2</sub> with isolated silica in lattice: An excellent photocatalyst for photocatalytic conversion of CO<sub>2</sub> into methanol under visible light irradiation. *J. CO<sub>2</sub> Util.* **2018**, *27*, 11–21. [[CrossRef](#)]
46. Zhang, H.; Tang, C.; Lv, Y.; Gao, F.; Dong, L. Direct synthesis of Ti-SBA-15 in the self-generated acidic environment and its photodegradation of Rhodamine. *J. Porous Mater.* **2014**, *21*, 63–70. [[CrossRef](#)]
47. Parvulescu, V.; Ciobanu, M.; Petcu, G. Immobilization of semiconductor photocatalysts. In *Handbook of Smart Photocatalytic Materials Fundamentals, Fabrications, and Water Resources Applications*; Hussain, C.M., Mishra, A.K., Eds.; Elsevier: Amsterdam, The Netherlands, 2020; pp. 103–140. [[CrossRef](#)]
48. Zhu, Q.; Lu, J.; Wang, Y.; Qin, F.; Shi, Z.; Xu, C. Burstein-Moss Effect behind Au Surface Plasmon Enhanced Intrinsic Emission of ZnO Microdisks. *Sci. Rep.* **2016**, *6*, 36194. [[CrossRef](#)] [[PubMed](#)]
49. Bouaziz, N.; Ben Mana, M.; Aouaini, F.; Ben Lamine, A. Investigation of hydrogen adsorption on zeolites A, X and Y using statistical physics formalism. *Mater. Chem. Phys.* **2019**, *225*, 111–121. [[CrossRef](#)]
50. Wu, Y.; Sun, K.Q.; Yu, J.; Xu, B.Q. A key to the storage stability of Au/TiO<sub>2</sub> catalyst. *Phys. Chem. Chem. Phys.* **2008**, *10*, 6399–6404. [[CrossRef](#)] [[PubMed](#)]
51. Li, L.; Wu, B.; Li, G.; Li, Y.C. N co-doping promoted mesoporous Au/TiO<sub>2</sub> catalyst for low temperature CO oxidation. *RSC Adv.* **2016**, *6*, 28904–28911. [[CrossRef](#)]
52. Chong, C.C.; Teh, L.P.; Setiabudi, H.D. Syngas production via CO<sub>2</sub> reforming of CH<sub>4</sub> over Ni-based SBA-15: Promotional effect of promoters (Ce, Mg, and Zr). *Mater. Today Energy* **2019**, *12*, 408–417. [[CrossRef](#)]
53. Aboukais, A.; Aouad, S.; El-Ayadi, H.; Skaf, M.; Labaki, M.; Cousin, R.; Abi-Aad, E. Physicochemical characterization of Au/CeO<sub>2</sub> solids. Part 2: The impregnation preparation method. *Mater. Chem. Phys.* **2012**, *137*, 42–47. [[CrossRef](#)]
54. Shin, H.; Choi, M.; Kim, H. A mechanistic model for hydrogen activation, spillover, and its chemical reaction in a zeolite-encapsulated Pt catalyst. *Phys. Chem. Chem. Phys.* **2016**, *18*, 7035–7041. [[CrossRef](#)]
55. Im, J.; Shin, H.; Jang, H.; Kim, H.; Choi, M. Maximizing the catalytic function of hydrogen spillover in platinum-encapsulated aluminosilicates with controlled nanostructures. *Nat. Commun.* **2014**, *5*, 1–8. [[CrossRef](#)]
56. Barakat, T.; Idakiev, V.; Cousin, R.; Shao, G.S.; Yuan, Z.Y.; Tabakova, T.; Siffert, S. Total oxidation of toluene over noble metal based Ce, Fe and Ni doped titanium oxides. *Appl. Catal. B.* **2014**, *146*, 138–146. [[CrossRef](#)]
57. Chinh, V.D.; Broggi, A.; Di Palma, L.; Scarsella, M.; Speranza, G.; Vilardi, G.; Thang, P.N. XPS Spectra Analysis of Ti<sup>2+</sup>, Ti<sup>3+</sup> Ions and Dye Photodegradation Evaluation of Titania-Silica Mixed Oxide Nanoparticles. *J. Electron. Mater.* **2018**, *47*, 2215–2224. [[CrossRef](#)]
58. Aljohani, M.M.; Al-Qahtani, S.D.; Alshareef, M.; El-Desouky, M.G.; El-Bindary, A.A.; El-Metwaly, N.M.; El-Bindary, M.A. Highly efficient adsorption and removal bio-staining dye from industrial wastewater onto mesoporous Ag-MOFs. *Process Saf. Environ. Prot.* **2023**, *172*, 395–407. [[CrossRef](#)]

59. Liu, W.; He, T.; Wang, Y.; Ning, G.; Xu, Z.; Chen, X.; Hu, X.; Wu, Y.; Zhao, Y. Synergistic adsorption-photocatalytic degradation effect and norfoxacin mechanism of ZnO/ZnS@BC under UV-light irradiation. *Sci. Rep.* **2020**, *10*, 11903. [[CrossRef](#)]
60. Zamani, F.; Rezapour, M.; Kianpour, S. Immobilization of L-lysine on Zeolite 4A as an Organic-Inorganic Composite Basic Catalyst for Synthesis of  $\alpha,\beta$ -Unsaturated Carbonyl Compounds under Mild Conditions. *Bull. Korean Chem. Soc.* **2013**, *34*, 2367. [[CrossRef](#)]
61. Zhu, H.; Yuan, X.; Yao, Q.; Xie, J. Shining photocatalysis by gold-based nanomaterials. *Nano Energy* **2021**, *88*, 106306. [[CrossRef](#)]
62. Cheng, D.; Liu, R.; Hu, K. Gold nanoclusters: Photophysical properties and photocatalytic applications. *Front. Chem.* **2022**, *10*, 958626. [[CrossRef](#)]
63. Yu, C.; Li, G.; Kumar, S.; Kawasaki, H.; Jin, R. Stable Au<sub>25</sub>(SR)<sub>18</sub>/TiO<sub>2</sub> Composite Nanostructure with Enhanced Visible Light Photocatalytic Activity. *J. Phys. Chem. Lett.* **2013**, *4*, 2847–2852. [[CrossRef](#)]
64. Lee, J.; Shim, H.S.; Lee, M.; Song, J.K.; Lee, D. Size-Controlled Electron Transfer and Photocatalytic Activity of ZnO-Au Nanoparticle Composites. *J. Phys. Chem. Lett.* **2011**, *2*, 2840–2845. [[CrossRef](#)]
65. Zhu, M.; Aikens, C.M.; Hollander, F.J.; Schatz, G.C.; Jin, R. Correlating the Crystal Structure of a Thiol-Protected Au<sub>25</sub> Cluster and Optical Properties. *J. Am. Chem. Soc.* **2008**, *130*, 5883–5885. [[CrossRef](#)]
66. Kogo, A.; Sakai, N.; Tatsuma, T. Photoelectrochemical analysis of size-dependent electronic structures of gold clusters supported on TiO<sub>2</sub>. *Nanoscale* **2012**, *4*, 4217–4221. [[CrossRef](#)]
67. Li, D.; Zhu, Q.; Han, C.; Yang, Y.; Jiang, W.; Zhang, Z. Photocatalytic degradation of recalcitrant organic pollutants in water using a novel cylindrical multi-column photoreactor packed with TiO<sub>2</sub>-coated silica gel beads. *J. Hazard. Mater.* **2015**, *285*, 398–408. [[CrossRef](#)] [[PubMed](#)]
68. Do, T.C.M.V.; Nguyen, D.Q.; Nguyen, K.T.; Le, P.H. TiO<sub>2</sub> and Au-TiO<sub>2</sub> Nanomaterials for Rapid Photocatalytic Degradation of Antibiotic Residues in Aquaculture Wastewater. *Materials* **2019**, *12*, 2434. [[CrossRef](#)] [[PubMed](#)]

**Disclaimer/Publisher's Note:** The statements, opinions and data contained in all publications are solely those of the individual author(s) and contributor(s) and not of MDPI and/or the editor(s). MDPI and/or the editor(s) disclaim responsibility for any injury to people or property resulting from any ideas, methods, instructions or products referred to in the content.